Three-Dimensional Constitutive Relations of Aligned Carbon Nanotube Polymer Nanocomposites

by

Daniel A. Handlin

B.A. Astrophysics
Harvard College, 2011

SUBMITTED TO THE DEPARTMENT OF AERONAUTICS AND ASTRONAUTICS
IN PARTIAL FULFILLMENT OF THE REQUIREMENTS FOR THE DEGREE OF

MASTER OF SCIENCE IN AERONAUTICS AND ASTRONAUTICS
AT THE
MASSACHUSETTS INSTITUTE OF TECHNOLOGY

JUNE 2013

Signature of Author ____
Department of Aeronautics and Astronautics
May 21, 2013

Certified by____
Brian L. Wardle
Associate Professor
Thesis Supervisor

Accepted by____
Eytan H. Modiano
Professor of Aeronautics and Astronautics
Chair, Graduate Program Committee

Three-Dimensional Constitutive Relations of Aligned Carbon Nanotube Polymer Nanocomposites

by

Daniel Handlin

Submitted to the Department of Aeronautics and Astronautics
on May 23, 2013, in partial fulfillment of the
requirements for the degree of
Master of Science in Aeronautics and Astronautics

Abstract

Variable and high volume fraction aligned carbon nanotube (CNT) polymer nanocomposites (A-PNCs) are fabricated by biaxial mechanical densification of the CNTs, followed by polymer infiltration via capillarity-assisted wetting using an aerospace-grade epoxy. These A-PNCs are mechanically tested in order to determine the full elastic constitutive relations of the material as a function of volume fraction. Prior to this work, only bulk compression or nanomechanical tests have been attempted due to the small size of the samples. Elastic stiffness results derived from optical strain mapping via digital image correlation are in agreement both with prior experimental nanoindentation measurements and finite element calculations that include the effects of waviness of the reinforcing CNT ‘fibers’. Results from longitudinal, transverse, and shear directed testing are shown for 0 to ~20% volume fraction aligned CNT reinforcement. Imaging via scanning electron microscopy and micro-computed tomography is used to establish morphology for structure-property relations. These are the first full elastic constitutive relations for non-isotropic aligned-CNT PNCs. Such relations are needed for modeling and understanding hierarchical nanoengineered composite architectures. Recommended future work includes more comprehensive shear sample testing and concerted modeling efforts to relate this experimental work to computational/theoretical studies of the nanocomposite properties as a function of morphology.

Thesis Supervisor: Brian L. Wardle
Title: Associate Professor

Acknowledgements

I have received a great deal of help from many individuals without whom it would not have been possible to complete this thesis.

First and foremost, my advisor Professor Brian Wardle has been a fantastic mentor from day one at MIT. He is always available to answer my numerous questions and many times throughout my project offered a new avenue to explore when I felt like I had run into a wall with one approach or another. From familiarizing me with the literature and teaching me the methodology and mindset of a successful researcher and scientist, this project could not have been completed without his guidance.

My colleagues in necstlab have been enormously helpful throughout my experiences. Sunny Wicks was always happy to share her enormous expertise in all aspects of the research process, whether dealing with curing epoxy, growing and densifying CNT forests, or more mundane matters like which classes to take or which of the bewildering array of forms at MIT actually need to be filled out. Ethan Parsons provided incalculable help in the aspects of digital image correlation and testing, and taught me a great deal about the mindset of a good scientist. He introduced me to the DIC literature and taught me to use Vic-2D as software that performs digital image correlation rather than a program where I press some buttons and hope that a black box process gives me a logical answer. He also helped to show me the importance of attention to detail- making sure that cameras are parallel to the ground, not 5 degrees from parallel, or measuring the exact distance of the camera from the samples being tested to the half millimeter- in many ways these ideas redefined how I was approaching the research. Roberto Guzman deVilloria got me started in the lab and provided my first introduction to growing CNTs, creating samples, and operating in the necstlab- his help was also enormously valuable as I was getting acclimated to MIT.

At NASA, Dr. Steve Scotti has been an excellent mentor who provided me with many useful ideas during my work at NASA Langley. William Johnson and Ed Townsley generously took time from their schedules to help me test samples in their 3-D digital image correlation setup, and Jae-woo Kim took time to take high-resolution SEM images of my forests.

My family has been with me each step of the way; both of my parents were a source of encouragement and enthusiasm at all times. My sister kept me focused on the bigger picture. And of course none of this could have been done without my best friend, without whom I surely would have lost my mind long ago.

Also, I would like to acknowledge the support of Boeing, EADS, Embraer, Lockheed Martin, Saab AB, Composite Systems Technology, Hexcel, and TohoTenax through the NECST Consortium, and NASA through the NSTRF fellowship.

Table of Contents

1. **Introduction**

2. Literature Review

3. Procedures

4. Results

List of Figures

List of Tables

List of Abbreviations And Symbols

CNT = Carbon Nanotube

PNC = Polymer Nanocomposite

DIC = Digital Image Correlation

SWNTs = Single-walled nanotubes

MWNTs = Multi-walled nanotubes

A- = Aligned

R- = Random

CVD = Chemical Vapor Deposition

c_{ijkl} = stiffness tensor elements

ε_{kl} = strain tensor elements

σ_{ij} = stress tensor elements

Vf = volume fraction

θ = PNC alignment angle

Chapter 1

Introduction

1.1 Overview

Nanomaterial-reinforced polymeric materials are of significant interest for their novel mechanical and transport (electrical, thermal, ionic, etc.) properties. Our group has previously demonstrated fabrication of aligned carbon nanotube (A-CNT) forests embedded in an aerospace-grade unmodified thermoset epoxy resin, forming an aligned-nanofiber polymer nanocomposite (A-PNC)[1]. Here, such samples are fabricated in dogbone shapes with CNT volume fraction varying between 0 and 20% for use in tensile testing to determine the full constitutive relations using digital image correlation techniques. This work reports on the testing and determination of these relations as a function of volume fraction including morphology studies to establish structure-property relations.

PNCs are of great interest for use in aerospace applications due to their ability to be tailored into multifunctional materials with superior mechanical and other properties[2]. Numerous studies have in recent years used CNTs as structural reinforcements in a wide variety of different polymers,[3] though morphologies of the CNTs found in these studies is typically random and at volume fractions only approaching 1%. The reported elastic modulus of single-walled CNTs (SWNTs) and multi-walled CNTs (MWNTs) has been reported by investigators to be potentially in excess of 1 TPa in both experimental[4,5] and theoretical[6,7,8] investigations. However, reported elastic moduli of CNT-based PNC materials has been significantly lower that expected from rule of mixtures and highly dependent upon CNT orientation and morphology. The PNCs have tended to have axial modulus similar to that of the original polymer matrix[3], on the order of several GPa. While previous studies have focused on incorporation of CNTs in epoxy matrices, these PNCs have generally featured randomly-oriented CNTs[9] (R-CNTs) and thus lack the potential benefits of CNTs of aligned morphology. Similar work with aerospace-grade polyimide matrices has also featured introduction of R-CNT reinforcement[10].

Our group has developed PNC fabrication methods that allow for creation of A-CNT PNCs with non-isotropic mechanical, electrical, and thermal properties along the different CNT axes, e.g., enhanced stiffness along the 'tangential' CNT axis direction[11]. This work is also interesting given the use of an unmodified structural aerospace epoxy as the matrix. PNC modulus in the CNT fiber direction measured with nanoindentiaion was found to be far below that calculated from micromechanics for perfectly straight CNTs but is consistent with rule-of-mixtures expectations given the observed CNT waviness in the samples.

Previous work by our group has studied the elastic modulus of these PNCs via use of nanoindentation[11] and has shown significant improvement compared with literature values for R-CNTs of the same CNT volume fractions. However, to date, the full three-dimensional constitutive relations of A-CNTs in an aerospace grade structural epoxy have not been reported. This study reports on efforts to develop these relations by use of these previously reported fabrication techniques in conjunction with digital image correlation (DIC), also known as optical strain mapping, thereby building upon previously reported work[12].

The fundamental goal of this work was to develop the first fully three-dimensional constitutive relations for A-CNT forests embedded in an aerospace-grade unmodified thermoset epoxy resin as a function of volume fraction. Many research groups have investigated the use of A-CNT PNCs for aerospace applications; an overview can be found in Dresselhaus et al. [51]. However, the vast majority of work done on PNCs to date has dealt with the use of PNCs with unaligned fibers[3]. Our group has previously demonstrated the fabrication of A-CNT PNCs[11] on a silicon substrate using a chemical vapor deposition (CVD) technique[11].

CNTs have a theoretical modulus of more than 1 TPa[52] and are thus much stiffer than other fibers such as carbon, glass or boron. However, like these other filaments, the CNTs must be embedded in a matrix for these properties to be usefully leveraged. They can also be grown along the fibers of a traditional composite [53]. Finally, it is possible to position CNTs between the laminae of a traditional composites, yielding interlaminar reinforcement and also potentially reducing crack propagation[54].

There are several reasons why A-PNCs are preferable to the use of randomly aligned polymer nanocomposites (R-PNCs). First, A-PNCs allow the use of diagnostic techniques, specifically X-ray imaging, to study the morphology of the CNTs, which can be correlated with the resulting macroscopic mechanical properties of the nanocomposite. Additionally, the use of aligned CNT forests allows the potential for increasing the functionality of the composites, depending on the applications and properties desired. Unlike R-PNCs, A-PNCs can be tailored to yield composites with specific properties of, e.g., strength, modulus, thermal conductivity or electrical conductivity. For example, the modulus along the CNT axis is much higher in aligned systems than reported R-PNC values[55]. Additionally, conductivity is much higher along the axis of A-CNT PNCs[56].

Significant work has been done to date regarding the use of randomly oriented CNTs in relatively low-strength polymers[57]. However, our group was the first to investigate the properties of A-CNT PNCs using an aerospace-grade structural polymer[11]. In this research the foundation laid by that work is built upon by introducing the use of digital image correlation (DIC; also known as optical strain mapping) to investigate the mechanical properties of the A-CNT PNCs in much greater detail. A schematic overview of the work is presented in Figure 1.1, showing representative sample orientations with CNT RVEs and example DIC results. Images of the PNC samples, along with their associated molds, can be found in Figure 1.2.

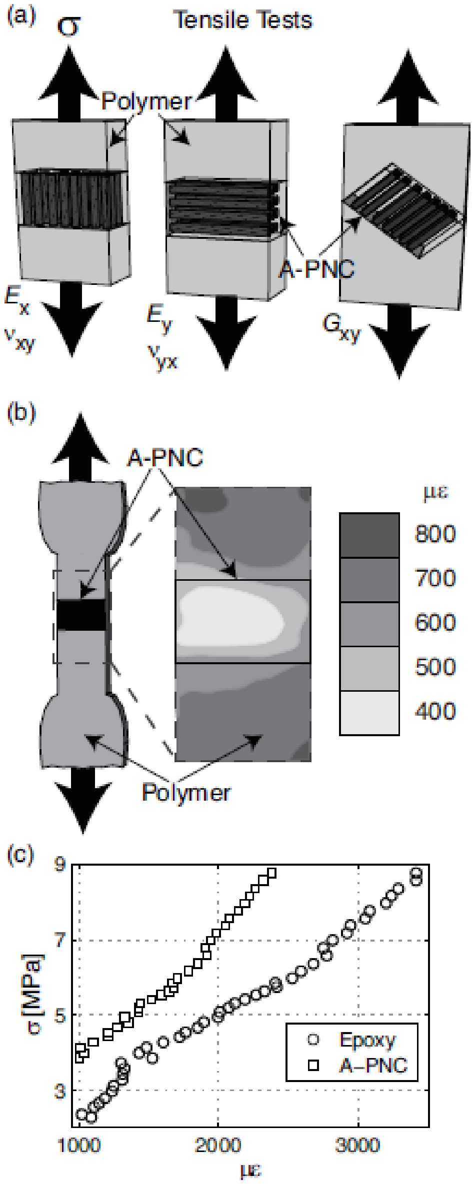

Figure 1.1 Schematic Overview of Methodology (Figure by Daniel Handlin and Itai Stein). a) Morphology of CNTs in PNC specimens, (left to right) longitudinal, transverse, shear. B) Representation of a PNC sample compared with a vector DIC image. C) Example stress-strain curve generated from DIC.

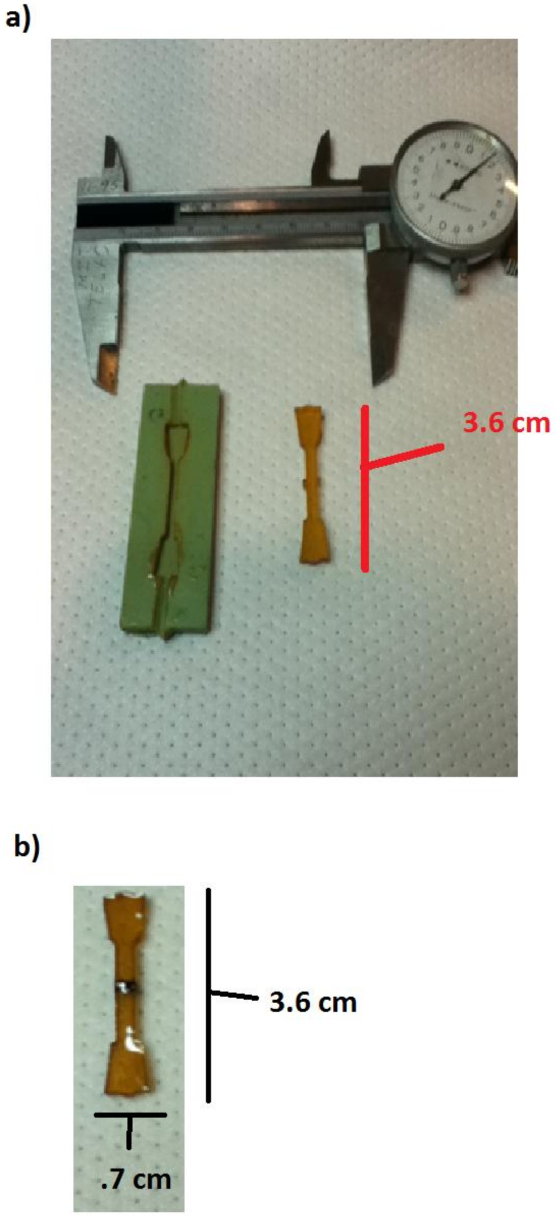

Figure 1.2 Images of Samples. a) Sample being taken out of mold. b) Image of an unspeckled sample.

1.2 Approach

The approach taken in this work was to design, create, and test A-PNC samples in a tensile testing machine and to use digital image correlation (DIC) to determine the local strain fields in the epoxy/CNT regions of the tensile testing specimens. By varying the morphology of the embedded CNT forests during the sample fabrication phase it was possible to create PNC specimens of CNTs embedded in RTM6 with the orientation and volume fraction of the CNTs variable as a function of volume fraction. A schematic of such an A-PNC RVE is shown in Figure 1.3.

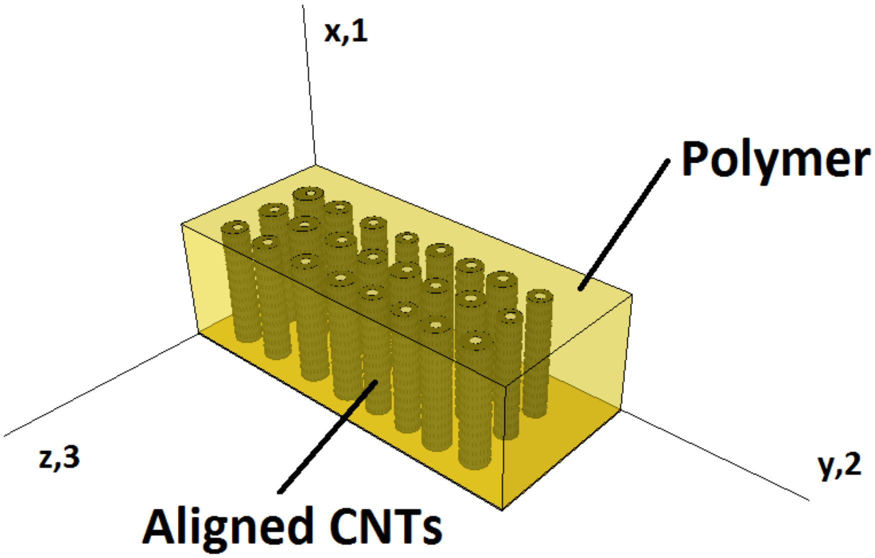

Figure 1.3 Schematic of Aligned CNT PNC (A-PNC) Material

CNT forests were grown in a CVD apparatus and wetted with the RTM6 epoxy; they were then inserted into molds to create the samples. These samples were polished and then marked in a manner suitable for DIC testing (“speckled”) using airbrushes. The samples were placed into a tensile testing machine and imaged during the tests; image sequences covering each test were subsequently analyzed using the program Vic 2D from Correlated Solutions, along with a DAQ output from the tensile testing machine that provided force (and therefore stress) levels. The localized strain field resolution capability provided by Vic 2D allowed for separate measurement of the epoxy and PNC regions of the samples and determination of the moduli of each PNC region as a function of volume fraction.

Chapter 2

Literature Review

2.1 Carbon Nanotube (CNT) 'Fibers'

Carbon nanotubes (CNTs) are cylindrical tubes of graphene approximately 1 nm in diameter but ranging in length from hundreds of nanometers to over 1 mm.[51] Identified by Iijima[19] in 1991, an explosion of research into CNTs has been present in the literature for the last two decades. Theoretically, CNTs offer extremely attractive mechanical, thermal, electrical, and strength-to-weight properties, offering unique and extremely useful applications ranging from aircraft deicing[20] to thin, lightweight, tough wires for the electronics industry[21] to the improbable space elevators, where their unique high strength-to-weight ratio makes them the only candidate for building such a structure from known materials.[22]

CNTs can be fabricated in the laboratory using three primary techniques: arc discharge, laser ablation, and chemical vapor deposition. The first of these is the arc discharge method. Iijima[19] first discovered CNTs in a high-current discharge between two graphite electrodes; the carbon is vaporized by the process and condenses to form both single- and multi-walled nanotubes. The second method commonly found in laboratory settings is laser ablation. In a reactor filled with a noble gas such as argon, a high-energy laser is used in this method to sublimate a carbon target; as in the arc discharge method, the carbon subsequently precipitates to form CNTs on the reactor walls.[23]

The third method, which is used in this work, is chemical vapor deposition (CVD). CVD involves the use of a substrate with a metallic coating; in this study, for example, a ~1 nm layer of iron was deposited onto a silicon wafer substrate for CNT growth during the CVD process. Several gases are then reacted inside a reactor or furnace, the most important of which for the CVD CNT growth process are a hydrocarbon and a reducing gas to react it with such as hydrogen or ammonia; other gases such as helium or argon can be used for flushing the lines of the system to remove air/oxygen. Full details of the CVD growth system used in this study will be presented later, but in general, the CVD process involves a chemical reaction that precipitates the carbon onto the metal nanoparticles from the metal film on the substrate, where it grows to form nanotubes. There are many different varieties of CVD systems, using various combinations of active gases, hydrocarbons, substrates and metallic coatings; additionally, there are a great number of ways in which the CNTs might be removed from the substrate after a growth period is completed[24]. CVD has some practical advantages over laser ablation or arc discharge methods as the CNTs are grown directly onto a substrate rather than on the walls of a reaction chamber. Full details of the particular CVD system used in this work are presented later.

Carbon nanotubes are of great interest to researchers due to their often extraordinary properties, especially mechanical and electrical. Theoretically, totally pure SWNTs can have a Young's modulus of >1 TPa along their axes, with a strength on the order of 200 GPa[11]. In practice, it is extremely difficult to grow, manipulate, or measure the modulus of individual SWNTs. Actual measurements of MWNTs produce modulus values on the order of 50 GPa[25] and strength values on the order of 30 GPa[61] due to deviations from a perfect cylindrical graphene structure (i.e. flaws in the structure). The strength of CNTs is particularly attractive for structural applications and ranks it among the strongest known materials. They are also extremely hard; SWNTs in fact have been observed to take on a superhard phase under elevated pressures with a bulk modulus well in excess of that measured for diamond (Popov et al.[26] reports a measured bulk modulus of these superhard phase nanotubes of 462-546 GPa), compared to 442 GPa measured for diamond.[62]

In practice, however, MWNTs also tend to suffer additional strength reductions due to shear interactions between the various cylinders that comprise the MWNTs.[27] As might be intuitively expected, the strength of CNTs is primarily found in tensile stress; due to their extremely large lengths relative to their radii or diameters, they buckle relatively easily under compressive loads.[28] Measurements with an atomic force microscope have also shown CNTs to have limited strength perpendicular to their longitudinal axes (i.e. CNTs are weak in radial compression).[29]

MWNTs and SWNTs are also well regarded for their extraordinarily high thermal conductivities. Pop et al. report[30] an experimental thermal conductivity for SWNTs of approximately 3500 W/mK in the longitudinal direction, while Berber et al.[31] have modeled a thermal conductivity for a different form of CNT in excess of 6600 W/mK, and Hone et al.[32] found experimental thermal conductivity values reaching 1750-5800 W/mK. This is far in excess of thermal conductivities of known metals. At the same time, other researchers have found very low thermal conductivities for CNTs perpendicular to their longitudinal axes[33] again leading to the prospect of intriguing applications for their use. Other remarkable properties of MWNTs include the ability for the nanotube cylinders to slide relative to one another with nearly no friction; this property has been exploited by researchers to create nearly frictionless bearings for nanoscale motors.[34]

CNTs have many potential applications that have been explored in the literature; some will be briefly examined here. The most frequently mentioned use of CNTs is in various structural applications, often via use as a filler for polymers, similar to the way in which chopped carbon fibers are mixed into polymers to create sheet molding compound (SMC), which finds considerable use in the automotive industry. Several researchers[35] have created long fibers of mixed, randomly aligned CNTs with a polymer covering that show promising mechanical properties. Some of the myriad other applications that have been discussed in the literature for CNT utilization have included “conductive and high-strength composites; energy storage and energy conversion devices; sensors; field emission displays and radiation sources; hydrogen storage media and nanometer-sized semiconductor devices; probes and interconnects”. [36]

Other frequently discussed uses of CNTs are as filler or strengtheners in bulletproof vest and body armor applications (often obviously mentioned along with Kevlar-reinforced polymers), and especially, space elevator applications. Space elevators are one of the most frequently mentioned ‘extreme’ applications of CNTs, but the disconnect between the frequency of such discussion and the actual technical readiness of CNTs merits brief discussion here. Space elevators are an idea to enable the facilitation of very low-cost space transportation first proposed by Tsiolkovsky in the late 19th century, and in their modern form by Yuri Artsutanov in 1959.[22] In such concepts, a satellite or platform in geostationary orbit about the Earth (or other body under consideration) is connected to the surface via an extremely long cable. “Elevator cars” ride up this cable to provide nearly-free rides for various payloads into orbit. However, the most important of the various longstanding engineering challenges for such a proposal has long been that no known material possessed the necessary tensile strength for fabrication of such a cable. Carbon nanotubes provide an exception to this, as they possess, in theory, the required strength to form such a structure.[22] Additionally, the use of CNTs could provide a way to provide electrical power running either up or down the cable due to their conductivity. However, needless to say here, fabrication of a nearly defect-free 36,000 km long CNT strand is very far beyond present technology, and thus CNT technology does not yet provide a feasible or realistic capability to construct a space elevator.

2.2 Polymer Nanocomposites

Polymer nanocomposites (PNCs) are polymeric materials which are reinforced, strengthened, or otherwise modified by the introduction and inclusion of carbon nanotubes. Due to significant and rapid recent advances in the computer-aided analysis and modeling of these materials, as well as the increasing use of STM microscopy, PNCs have found increasingly common use both in the laboratory and in applications over the last two decades.[36] At a very basic level, even natural substances such as human bone or marine life shells can be considered nanocomposites, given their use of nanoscale-sized particles in a larger matrix[36]; the automotive industry has also been using nanocomposite reinforcement for nearly 20 years with a strong increase in the desirable mechanical, thermal, and electrical characteristics of the materials being altered.[36] Generally, those materials most often used as the nanoscale phase in PNCs "include, nanoparticles, nanotubes, nanofibers, fullerenes, and nanowires… [i]n general, these materials are classified by their geometries [8]; broadly the three classes are particle, layered, and fibrous materials [7,8]". [36] CNTs are an example of a fibrous nanoscale material in this scheme.

As with other forms of composites, the interfacial bond between the CNTs and the polymer matrix, as well as the dispersion of the CNTs themselves, is vital for production of composites with improved multifunctional properties over the non-reinforced matrices; and indeed, an improperly prepared PNC can have significantly diminished mechanical and other properties relative to the unreinforced material.[37] Two key effects create significant difference between PNCs and more traditional macroscale composites with micron-scale fibers and fillers: the vastly increased relative surface area and associated interfacial bonding regions between the CNTs and the polymer matrix, and the manifestation of various quantum mechanical effects due to the extremely small scale of the CNTs.[36]

In general, the methods used to manufacture PNCs have to date employed a variation of one of the commonly used techniques for fabrication of other forms of composites; to wit, as explained by Hussain et al. [36], "wet lay-up, pultrusion, resin transfer molding (RTM), vacuum assisted resin transfer molding (VARTM), autoclave processing, resin film infusion (RFI), prepreg method, filament winding, fiber placement technology, etc."[36] Unlike CNT fabrication, there does not seem to be any relatively small set of methods generally accepted for use in the fabrication of PNCs, whether in the laboratory or in industry for use in PNC applications.

There are two fundamental or 'philosophical' approaches to creating CNT-PNCs in particular; the attempt to use CNTs to create a fiber independently of the use of a matrix, and the dispersion of CNTs within a matrix.[36] The thinking behind the former approach is that it would allow fabrication of fibers with properties that might approach those of the unmodified nanotubes, which are, as discussed above, much stronger than those nanotubes that have actually been produced or dispersed into PNCs. However, as with the CNTs themselves, it has proven extremely difficult to fabricate such structures without numerous defects that significantly reduce the strength of the resulting fibers, and thus dispersion into a matrix has to date remained the dominant approach.[36]

While dispersion of CNTs into a polymeric matrix has proven to be experimentally tractable, measured properties of such PNCs has to date fallen well short of theoretical expectations. Some researchers have found no improvement at all in PNCs over the unreinforced materials[38],while other have found only marginal improvements in modulus of a few tens of percent[39] or slightly larger improvements in thermal[40] or electrical properties.[39]

In general one of the most difficult challenges in fabrication of PNCs with desirable properties is achieving a relatively uniform dispersal of the nanomaterial throughout the polymer matrix and avoiding agglomeration; this is made much more challenging by the fact that the CNTs tend to attract each other due to van der Waals forces acting between the nanotubes; this is especially problematic for SWNTs due to their much higher surface area relative to MWNTs.[36] Uniform CNT dispersion is important in PNCs whether they are being used for structural or thermal/electrical applications. In the former case, spreading of CNTs throughout the composite is necessary for optimal load transfer between the polymer and the CNTs; the use of aligned CNTs, relatively rare in the literature, is also extremely helpful in this regard[36]; in the latter, good dispersion is needed as it “can assist with the realization of a network for conductivity of electrical and thermal energy”. [36] Numerous techniques have been explored in the literature in an attempt to achieve better dispersal of the nanotubes in the various polymer matrices that have been used. As Hussain et al.[36] explain, "Researchers have used many different techniques in an attempt to disperse nanotubes in polymer matrices including solution chemistry to functionalize the nanotube surface [219–223], the use of polymers to coat the nanotube surface [224], in situ polymerization of the nanocomposite [225,226], ultrasonic dispersion in solution [181,227], melt processing [11,228–232], the use of surfactants [233,234], electrospinning [235], electrode chemistry [236], and gelation/crystallization [237]".[36] However, to date, none of these methods has proven to be completely or consistently successful.

Much of the work reported in the literature to date has involved the use of thermoplastic polymeric systems rather than the far more common thermoset materials used for aerospace applications, since they are perceived by many researchers as being somewhat easier to work with in laboratory setting for this particular use[36], although some thermoset work has also been performed.[41] Much of this work encounters the problem of the cross-linking process in the epoxy interfering with the optimal dispersion of the nanotubes.[36] The area of the interfacial boundary between the nanotube and the polymer matrix is a research topic of special interest. It is in fact not known the degree to which CNTs bond chemically with polymer matrices, and if so, whether such bonding has the effect of altering the properties of the polymer or CNTs.[42] Additionally, a great deal of modeling work has shown that MWNTs are likely to have far more defects than SWNTs;

given that MWNTs tend to be easier to fabricate, this lends an additional challenge to both the processing of high-quality CNTs for use in PNCs and to the problem of understanding the interfacial behavior between CNTs and their polymer matrices.[43]

2.3 Digital Image Correlation for Local Strain Measurement

Optical strain mapping, usually referred to in the literature as Digital Image Correlation (DIC), is the method used during this study to calculate strain values. DIC is fundamentally a subdiscipline of image matching, which is itself a topic of the broader field of computer vision problems.[44] DIC is distinguished from other image matching approaches primarily by two factors: a very high resolution (submicron level) and an almost exclusive use in engineering and scientific applications such as that explored here.[44]

Qualitatively, the basic overall idea of DIC as applied to optical strain mapping is straightforward. The first step is the application of a speckle pattern consisting of hundreds or thousands of small dots over the area of interest (AOI) in question. Strain is then applied to the sample while the AOI is continuously imaged by a digital camera connected to a computer. By imaging the pattern of dots as they move apart from each other while strain is applied to the sample, and computing the precise motion of the dots relative to each other from image to image, it is possible to perform a computer analysis that determines the amount of strain that must be present on each visible portion of the AOI in order to produce the observed speckle pattern displacements (though to be more precise, it is actually the gray value of the pixels that is tracked and correlated rather than the dots per se – see[44] for more detail on this issue). We will here focus on a very basic overview of the theory behind DIC.

The speckle pattern must be applied to the sample in order to address the 'correspondence problem', which is simply a formal mathematical statement that without a certain threshold number of points that move relative to each other, it is not possible to find a unique solution to the motion of the AOI during the strain test; the very large number of dots applied (~20000) during the speckling of the DIC samples is necessary to avoid the correspondence problem (or its related special case, the "aperture problem" [44]).

If the speckle pattern is not a small pattern of dot-like structures, it can be far more difficult to extract meaningful or reliable strain information from the available imaging of a given test. If, for example, a grid of lines is used instead of a pattern of random dots, it is only possible to determine motion of the sample in directions perpendicular to the line assuming a finite field of view or aperture (this is the aforementioned 'aperture problem'). [44] It is also necessary to limit consideration of the possible locations of a pixel that has moved between subsequent DIC images to a relatively small area within the aperture, or else the mathematics of the problem very rapidly become intractable, since, as Schreier et al. explains, [44] "it is generally not possible to find the correspondence of a single pixel in one image in a second image. Typically, the gray value of a single pixel can be found at thousands of other pixels in the second image, and there is no unique correspondence". [44] However, consideration of this small area necessarily requires a small area, thus reintroducing the aperture problem which as discussed makes the use of speckle patterns like uniform line grids unfeasible.[44] Therefore, a random pattern of slightly nonuniform dots provides the ideal speckle pattern for use in DIC –since a nonrandom pattern can lead to the possibility of misidentifying the proper correspondence of points between images, necessitating the use of a larger aperture, which negatively impacts resolution.[44] A schematic of the DIC process can be found in Figure 2.1.

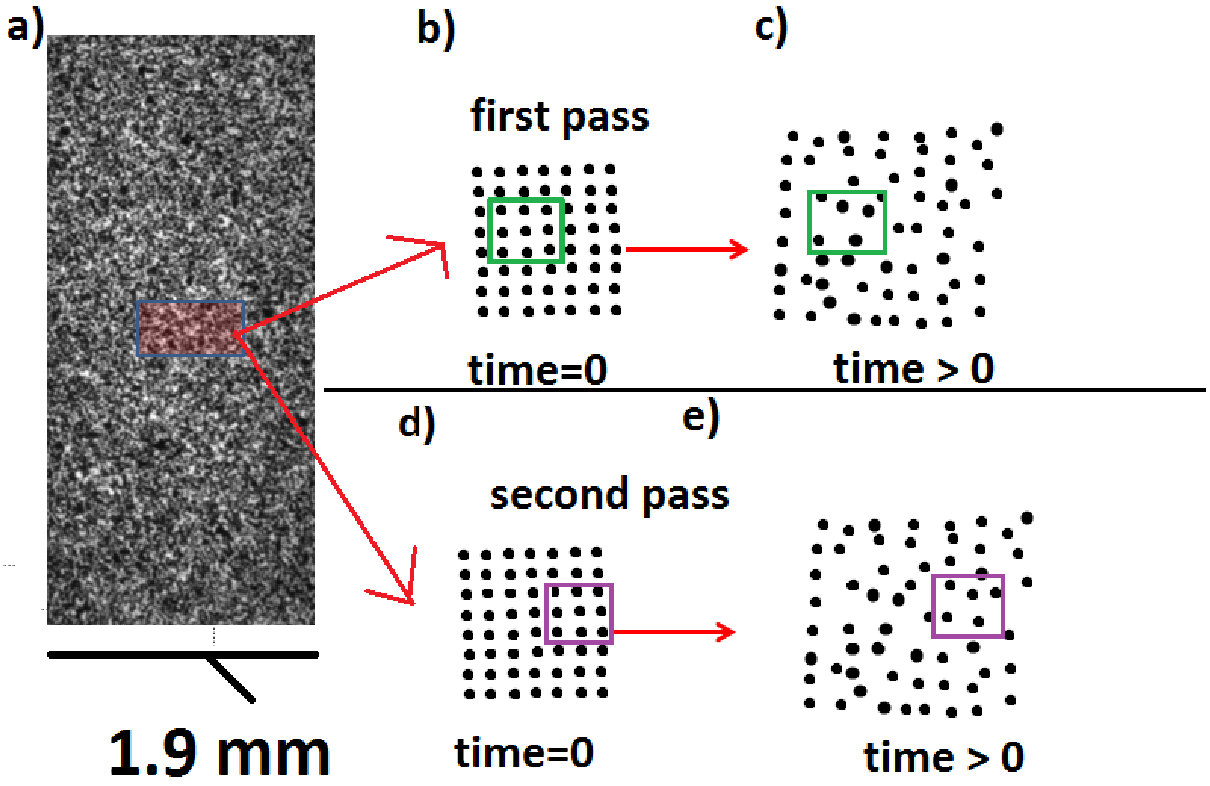

Figure 2.1 Schematic of Digital Image Correlation (DIC) Process. a) Section of a DIC sample with a box drawn to represent a zoomed in region. b) Schematic representation of the speckle pattern, where the green box represents a single subset. c) Deformed pixels in the subset from b) at a later time. The DIC software calculates a strain field in this subset based on how the speckles have moved relative to each other between b) and c). Note that only the speckles within a single subset will be compared to each other between b) and c) – i.e. the displacement field inside the green box is calculated only by reference to

other features within that box (the subset). By stepping subsets over the whole field of view the software builds up a strain map of the whole specimen. This is shown in d) and e), where the same steps as b) and c) are shown, but now the subset has been stepped to the next region. d) The subset is now stepped by an amount specified by the user to the next part of the sample. e) New subset analyzing the displacement at a later time, as in c). After enough passes are done to cover the entire sample, the displacement field for the whole specimen can be generated.

It is worthwhile at this juncture to discuss the issue of practical application of speckle patterns, a question which is often glossed over in the literature but is of great practical concern when preparing DIC tests. Several techniques can be used for applying a speckle pattern to a sample depending on the nature and size of the sample as well as the desired speckle size. On extremely large panels it is possible to simply hand paint a random pattern of dots onto the test item. However, most samples on which DIC is used are much smaller and it is necessary to apply dots of micron or submicron size in order to obtain strain pattern results of acceptable quality. Some possible techniques that have been utilized to apply speckle patterns include airbrushing dots of paint onto the specimen (the method ultimately used for this study); spray painting directly from a spray paint can [46] (as will be discussed, this method was tested and rejected for this work); using a straw to blow toner across the surface[47] (also tested and rejected); and printing of a speckle pattern directly onto the sample being tested. [48]

There are numerous different ways to calculate the motion of pixels in a DIC problem, many of which can lead to nearly identical answers despite completely different mathematical approaches. The software used in this study was Correlated Solution’s Vic

2D, the algorithm of which has been expanded upon elsewhere[49], and was originally published in the landmark paper by Sutton et al. [45] (it has since been optimized). To summarize the method used by Vic-2D extremely briefly, the program relies on the Newton-Raphson approach to partial differential corrections.[50] First, each pixel in the image is converted to a grayscale value. The basic idea is then to compare a subset of pixels as it moves between each set of images (this is the same entity that we referred to as an 'aperture' above). The precise correlation function used to connect subsets between images is eq. 4 from Sutton et al. [45] , in which the parameter S is to be minimized. Ultimately the goal of the program is to optimize the values of the other parameters in order to find the smallest possible value of the parameter S[45], with the Newton-Raphson method being the particular mathematical approach used to perform this optimization; it can be shown that the algorithm allows for image correlation to subpixel accuracy. Far more detail on the specifics of this algorithm can be found in the other sources referenced. It is also possible to extend this algorithm to measure displacement and strain in the third dimension (toward and out of the plane of imaging) by use of two cameras, as was done in this work for the Vic 3-D analysis. This essentially uses the same algorithm as Vic 2-D (indeed, Vic 2-D is a downgraded version of Vic 3-D with certain modules deactivated) but adds an additional step called stereo correlation to the analysis. [63]

Chapter 3

Procedures

3.1 Aligned CNT Polymer Nanocomposite (PNC) Fabrication

3.1.1 PNC Fabrication

The first step in creating the tensile dogbone samples used in this project was growth of CNT forests in a 1” diameter CVD furnace optimized for growth of long, easily delaminable nanotube forests. The nanotubes were grown using a process previously developed in our research group[58], though significant time and effort was put into modification and study of this growth method due to problems encountered during its use for this study, as will be discussed later.

Creation of the polymer nanocomposite samples involves a number of steps. CNT ‘forests’ were grown on rectangular Si wafers covered with a thin film of 1 nm Fe and 10 nm Al_2O_3 using a chemical vapor deposition (CVD) process. Beginning as a round 6-in piece, the wafers were manually cut into smaller rectangular pieces by hand after deposition of the coating; the process of preparing the wafers is described in detail by our group in[58] so fabrication of the wafers will not be elaborated upon further here.

The CNT forests were grown by placing the treated silicon wafers in the "1-inch (25.4 mm) furnace", a two-zone, atmospheric pressure, Lindberg/Blue furnace using a quartz tube for growth. Three gases are used in the growth process: helium (He), ethylene (C2H4), and molecular hydrogen (H2), with the helium being used primarily for flushing. The gas flow and furnace temperatures were controlled by the Ansari computer program on a desktop set up adjacent to the furnace. The sequence described here will be the final growth sequence as evolved through the testing performed during the course of this study; the nature of those tests and the effects they had on changing the preferred growth cycle will be discussed subsequently.

The process was divided into several steps. The first step involved purging the gas lines by flowing all three gases through the system at ambient temperature; this phase took two minutes. Next, there was a step in which helium was flushed through the lines prior to the start of a new growth cycle; in the final growth cycle this period totaled ten minutes with the helium flow set at 400 sccm. During the next phase, the temperature of the furnace was ramped up to 700 deg C. Once this temperature was recorded by the thermocouples inside the furnace, hydrogen was flowed through the lines for two minutes, followed by the introduction of ethylene to the mixture. In the heated hydrogen-ethylene mixture, CNTs grow very rapidly; in previous work done by our group, this growth rate was found to be on the order of 0.5-2 microns/sec.[11]

The full details of the growth process remain to be fully understood and characterized. However, the essentials can be outlined here insofar as they are known. Once the highest temperature is reached, the iron oxide-on-alumina catalyst is coarsened into iron nanoparticles in the reducing environment, which serves as sites that can initiate CNT growth.[54] The ethylene is broken down ('cracked') at the high ambient temperatures that are present in the tube, and the carbon atoms that had been part of the ethylene molecules serve to provide the carbon that ultimately makes up the resulting CNTs.[54] It is worth noting that the exact mechanism by which the CNTs are formed is not well understood, but is thought to involve the formation of a small mound or 'cap' of carbon on the iron nanoparticle surface to form a CNT nucleus, which subsequently grows perpendicularly to the surface of the catalyst. [54] This period was continued for 12.5 minutes in the final iteration. This was then followed by a 5 minute "easy delamination" period, in which hydrogen was flowed through the system at temperature in order to delaminate the base of the CNTs from the silicon wafer, effectively reducing them, in order to separate the forests after removal from the furnace. Finally, the hydrogen and furnace heater were shut off and the system allowed to cool. The furnace was generally opened once the temperature dropped below 600 deg C; the helium flow was stopped when the temperature dropped below 200 deg C; and the tube was opened to ambient when the temperature fell below 150 deg C.

The CNT growth cycle as outlined above was only evolved after a lengthy period of troubleshooting various problems that were encountered with the practical realization of this process. In theory, this process would reliably yield very long (>1 mm), easily delaminable CNT forests; in practice, all three of these aspects (reliability/repeatability, length, and delaminability) required significant work on and modification of the parameters of the growth system.

The key problem centered around reliably and repeatedly obtaining forests of the desired length. While the growth recipe had been tailored to provide, in theory, forests of 1 mm or greater lengths, in practice, growths obtained during the first several months of use rarely exceeded half this length, and lengths were also extremely variable across the length of the growth tube, and even individual wafers, in a way that was not consistent or understood. Numerous steps were undertaken in an attempt to characterize this problem and to increase the length of the nanotube forests as the properties of the CNT furnace were systematically explored.

The first step was experimentation with the use of a preheater to break down or ‘crack’ some of the ethylene gas before it entered the growth tube, which had not initially been connected to the system. While introduction of the preheater did not show any immediately obvious or marked improvements in the growth results, its use was retained in all future growths given that the theoretical understanding of the CNT growth process as described above involves significant cracking of the ethylene prior to the inclusion of its molecules in growing CNT forests. The preheater operated at 800 deg C.

Subsequently a ‘water bake’ was experimented with. This was a step that involved first opening the ends of the quartz growth tube. Next, 5 mL of water were injected on each end of the tube using a syringe. The syringe was then discarded. The tube was tilted at 45 degrees to the left and right in order to let the water flow through as evenly as possible through the tube. The tube was then ‘baked’ with both caps off at 200 deg C for 10 minutes, or until all the water had visibly evaporated if the former time was insufficient to accomplish this goal. When the water bake was performed on a new tube, there was a marked improvement in growth that would last for up to three growth cycles; CNT forests grown in such water-baked new tubes would be extremely long (up to 1.5 mm) and easily delaminable. However, within three or less successive growths, the improvement would no longer be evident, and subsequent water bakes in fact appeared to have a detrimental effect on CNT forests, often apparently contributing to cementing of the CNT forests into the wafer and making them nearly impossible to delaminate. Additional water bakes performed up to two weeks after the initial one appeared to have no discernible effect in improving the CNT growths, and often (in approximately 50% of cases) had this cementing effect. The reasons for this behavior remain unclear, but as a result the use of water bakes was discontinued except for brand new tubes. Exterior humidity is thought to be a confounding factor, but more data would be needed in order to confirm or refute this hypothesis and the effective of the humidity on the water bake effectiveness.

The position and number of the wafers within the tube was also experimented with. The wafers were generally rectangular after cutting with side dimensions on the order of 5-10 mm. Initially, four wafers were used, spaced symmetrically about the exact center of the furnace (which was carefully measured with a ruler and then marked on the furnace itself), with approximately 2 cm separating each of the four wafers from their nearest neighbor.

The number of wafers, and their locations relative to each other, were also varied as a parameter. Initially, as discussed, four wafers were used simultaneously for growths. The use of greater numbers of wafers- five or six- had a marked detrimental effect on the length of the CNTs. Often for especially large numbers of wafers (i.e. six), there would be a pattern in which the wafers on the edges would have the longest growths, and the wafers in the center of the group would have little or even no visible CNT growth at all. This pattern was not usually seen with smaller numbers of wafers. However, the five-wafer growths still produced noticeably shorter CNT forests than those with four or fewer. Conversely, however, the use of less than four wafers did not appear to have a positive effect on growths; attempts were made with both single wafers and three wafers. Therefore, after this experimentation, four wafers was retained as the ideal number for a growth.

The positioning of the wafers relative to each other was also moved. Positioning the wafers especially close to each other (<.5 cm) tended to promote a growth pattern similar to that discussed above for the six wafer case, where the wafers on the edges of the group would have relatively longer growths, while those toward the middle would be severely depleted or even bare of CNTs. This may have been due to some sort of interaction in the gas above the wafers that is not currently understood. At the same time, increasing the distance between the wafer edges up to 5 cm appeared to have no effect on the CNT growths, except inasmuch as it might pushed the leftmost wafer out of the optimal (near-center) growth zone as discussed above.

Numerous other parameters are thought to affect the growth of the CNTs within the 1-inch furnace. One of these is humidity. This was measured by a portable sensor in the growth room and was recorded prior to each growth; it usually was in the range of 32-34% as recorded by this sensor. This could not be controlled independently except to the extent that the water bake, discussed above, affected the water content inside the tube. Additionally, the tubes degrade from their new state in a somewhat unpredictable way that is not understood; it was thought that the buildup of ‘sooty’ carbon products within a new quartz tube after some weeks of use is in some way beneficial to the CNT forest growth process, but no evidence of this was found during the course of this work. It was observed, however, that using a tube for more than three growths immediately following one another would lead to significantly shorter forest lengths; it was usually necessary to wait overnight after conducting this number of growths in order for the tube to ‘recover’ to its normal state and again produce CNTs of normal length. It has been speculated that this behavior may relate to the slow absorption of water by the tube overnight and its use during the growth process; however, this interpretation of events is considered suspect given the results of the water bake attempts discussed above.

The CNT growth time was also modified. In general, a longer CNT growth time will yield longer forests, but excessively long times (greater than ~15 minutes) can lead to cementing of the forests into the wafers, which makes them impossible to remove for use. It was found that growth times of 15 minutes or longer usually led to this cementing, while 10 minute growths led to noticeably shorter CNT forests; 12.5 minutes was adopted as a compromise. The ‘easy delamination’ routine following each growth period also varied in time, eventually being set at 7 minutes. Longer ‘easy delaminations’ did not yield CNTs that were notably easier to delaminate.

More generally, it should be noted that the behavior of the CNT growth apparatus was extremely difficult to study because of the very large number of variable parameters which may have had an effect on the growth process. While studies may have been performed to change, e.g., wafer spacing, the effect of confounding factors such as the history of the tube use that day or the changing ambient humidity could not be easily controlled for given the time constraints of this study; nor was it possible to exactly control for variables such as slightly altering silicon wafer sizes or changes in the ambient temperature of the laboratory. In addition, the 1 inch furnace is used by other users, each of whom is introducing various other substances into the tube which may interact with these other parameters in unpredictable ways. Given that the goal of this work was not primarily to characterize the CNT growth process and furnace in itself, these factors did not receive sufficient study, and in practice, forests grown under a variety of different circumstances were grown and used for sample creation providing simply that they were long enough. However, as has been made clear here, a detailed, well controlled parametric study of the CNT growth process is clearly in order.

The next step after CNT forest growth was the fabrication of the PNC dogbone specimens for speckling and tensile testing. This step entailed the use of several subprocesses.

The CNTs first had to be delaminated from the silicon wafers. Once the ‘easy delamination’ procedure had been run, as it was part of the CNT forest growth process as discussed above, then CNT delamination in principle involved touching one of the edges of the CNT forest with a razor blade; the forest would then pop off the silicon wafer in a single piece which could then be transferred to the densification apparatus, the next stage of the process. However, this process only actually occurred in that ideal way on a single occasion. In every other case, some physical forcing of the razor blade into the CNT base was required to physically remove it from the silicon wafer. In those cases where the CNTs had been cemented to the wafer, as in some of the water bake cases discussed above, or after excessively long growths, then this act of attempting to delaminate the forests would physically tear and destroy them, rendering them unusable. Otherwise, careful and judicious use of the razor blade in an attempt to slowly remove the CNT forests from the wafers proved workable; it was found that slowly shearing the razor blade back and forth as it proceeded along the length of the silicon wafer usually produced a relatively clean delamination. In each case, once the delamination was complete, the CNT forest was transferred on the wafer to the densification apparatus.

The next subprocess was the manual mechanical densification of the CNT forests. A schematic illustration of this process is shown in Figure 3.1. Densification involved the use of a Teflon densifying apparatus created specially for this purpose. [1] The delaminated CNT forests were transferred on the razor blade to the top of the densifier. A clear cover was then placed over the forest to hold it in place. Next, two handheld 'squeezers' were used to physically push the CNT forest in two dimensions down to a smaller size. In this way, CNTs of any volume fraction desired could be produced up to about 20%, beyond which it became impossible to manually compact the CNTs any further. The volume fraction was measured by assuming that the CNT forests come out of the 1-inch furnace at approximately 1% Vf; the area of the squeezed CNT forest was then divided by the area of the original wafer, which was saved, in order to find the volume fraction (i.e. a final forest area of 20% of the original wafer size was assumed to be equivalent to a 5% Vf CNT forest). The size of the squeezed forest was measured using a caliper laid over the clear piece of the densifier while the CNT was in the densification apparatus, while the wafer size could be measured later, also using a caliper. The silicon wafers were generally not perfect rectangles, so these measurements are likely subject to some error; of course, the CNT forests themselves are unlikely to be at exactly 1% Vf coming out of the furnace, lending additional uncertainty to the Vf measurements.

On rare occasions, a part of the CNT forest would catch or tear on part of the densifier during the densification process; such CNTs were discarded. This was likely due to slow degradation of the Teflon surface of the densifier with extended use over time. Otherwise, this process yielded relatively few problems.

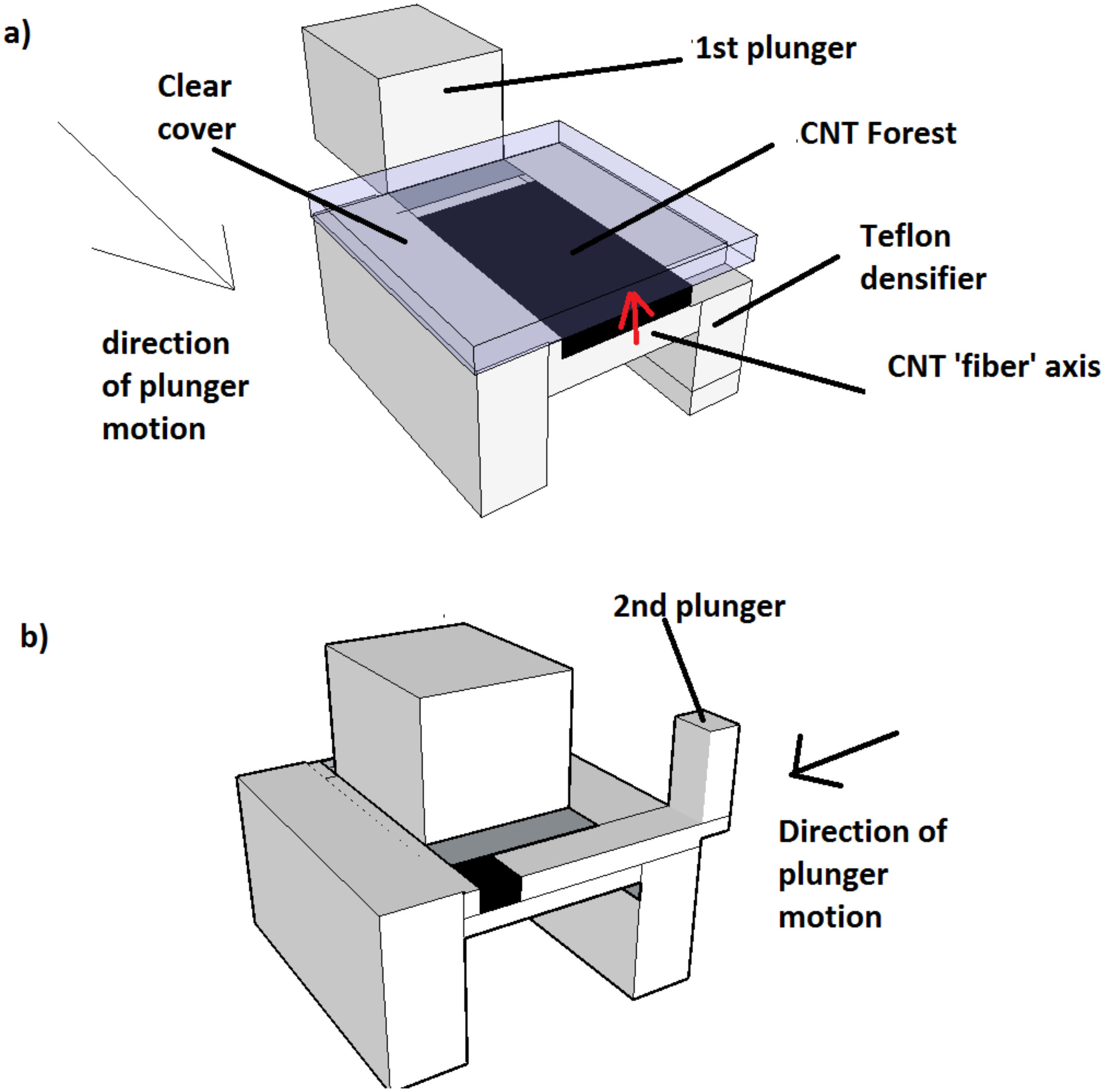

Figure 3.1 Schematic of Densification Process. a) Initial insertion of CNT Forest and densification in first axis. b) Second step, densification in axis perpendicular to that acted upon in a.

The mechanically densified CNT forest was now wetted using the chosen epoxy, RTM6. RTM6 is an aerospace grade structural epoxy produced by Hexcel. The two-part system had previously been mixed. Usually a given jar had to be degassed before use, which involved placing the epoxy in a vacuum jar and then heating it in an oven to 80 deg C. The jar, under vacuum, was held at temperature for 30 minutes; air was then let back into the jar to let the gas bubbles escape. After degassing of an individual jar of epoxy, it was ready for use. The epoxy in its frozen or room-temperature state is extremely viscous and essentially solid, so it had to be heated before use in PNC creation. The jar of epoxy was placed on top of the Lindberg/Blue M oven, on top of the opened aperture intended for use as vacuum line exhaust. The oven was then heated to 90 deg C. Thus, each epoxy jar was heated from the bottom. After a period of time when the epoxy was qualitatively judged to be sufficiently liquid for use- usually approximately 20 minutes- it was removed from the oven surface and brought to the PNC work area where the CNTs had been densified. The epoxy jar was put on a hot plate set to 90 deg C in order to keep the epoxy liquid.

In addition to the Teflon densifier itself, there existed another piece to the apparatus whose function was to provide a surface for curing of PNCs, shown in Figure 3.2. This Teflon surface had several grooves or notches cut into it; small squeezers could be fit into these grooves to provide a pocket and a surface to allow for pooling of epoxy to cure PNCs. A tiny quantity of RTM6 was poured from the heated jar into an aluminum dish, and then this dish was used to carefully pour the RTM6 into the space created by the squeezers.

Next, the densified CNT forest was picked up from the densifier using tweezers, and rested on top of the RTM6 surface. As the RTM6 wetted the CNT forest from the bottom up, the CNTs would slowly sink down into the bottom of the epoxy pocket (very gently assisted by tweezer pushes). If additional CNT forests were to be cured simultaneously on the same surface, the Teflon piece would be put on the hot plate also; otherwise, it would be taken to the oven for the first cure.

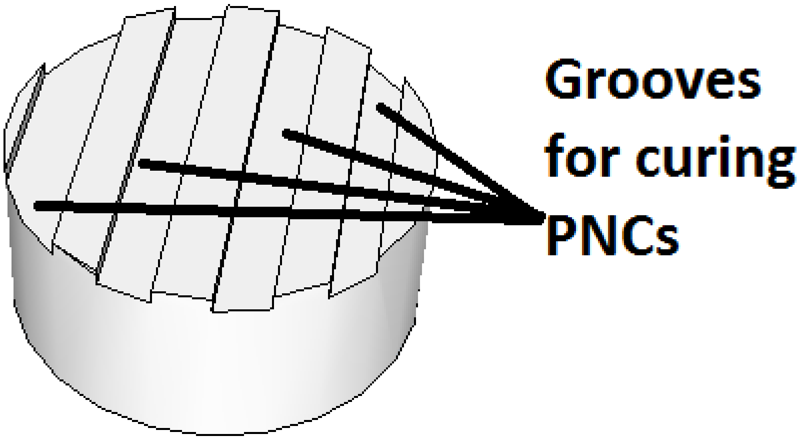

Figure 3.2 Diagram of Teflon piece used for curing A-PNCs.

This cure began with the oven preheated to a temperature of 80 deg C. Once this temperature was reached, the PNC curing piece was inserted in the oven. This first cure held the oven at 160 deg C for a total of 75 minutes. This cure solidified the PNC into a single, small hard block of CNTs in the RTM6 epoxy, ready for further manipulation within the tensile dogbone molds to be discussed below.

In practice, this step was extremely difficult and resulted in the loss of many CNTs. Numerous methods of wetting the CNTs with resin were attempted before settling on the technique outlined here. Originally, this involved physically forcing the densified CNT forest into the aluminum dish holding the epoxy in an attempt to wet the forest. However, the forces that this put on the forests destroyed a very large number of them; while it had previously been introduced to this author as the preferred method for CNT wetting, it was soon abandoned. For some time this was replaced by allowing the CNTs to sit in the heated aluminum dish with epoxy, and then transferring the wetted forest to the curing surface. However, this too entailed the lost of many forests during the removal stage from the aluminum dish. Finally, the method discussed here- wetting the CNTs directly on the curing surface- was settled upon, as it allowed wetting of the CNTs without the need of dragging them through the epoxy and thus exposing them to the large forces that frequently tore the wetted forests in the approaches where this was necessary. This step was originally the result of the loss of a very large number of wetted forests, and was a roadblock to the creation of PNCs- especially those with smaller Vf, and their correspondingly larger surface area and susceptibility to drag forces- for some time.

3.1.2. Creation of Tensile Testing Samples

The next step was removal of the now-cured PNCs from the oven and their subsequent inclusion in dogbone specimens for tensile testing. This was accomplished by the use of silicone molds that had been created by pouring a two-part silicone elastomer system into a mold negative. The PNC was placed in the center of the mold, physically restrained in place by the sides of the mold (if this latter step were not done, the PNC block would rotate out of position during the following cure cycle, likely due to convection within the epoxy- this was observed on many occasion, resulting in unusable samples). Next, the epoxy, heated to 90 deg C in the same way as previously described, would again be poured into an aluminum dish. The epoxy in this dish would then be poured across the empty mold with the PNC in the center. The epoxy would flow to fill in the gaps in the mold and would then be taken directly to the oven for curing. In this case, the cure was for 120 minutes at 180 deg C. The process is illustrated in Figure 3.3.

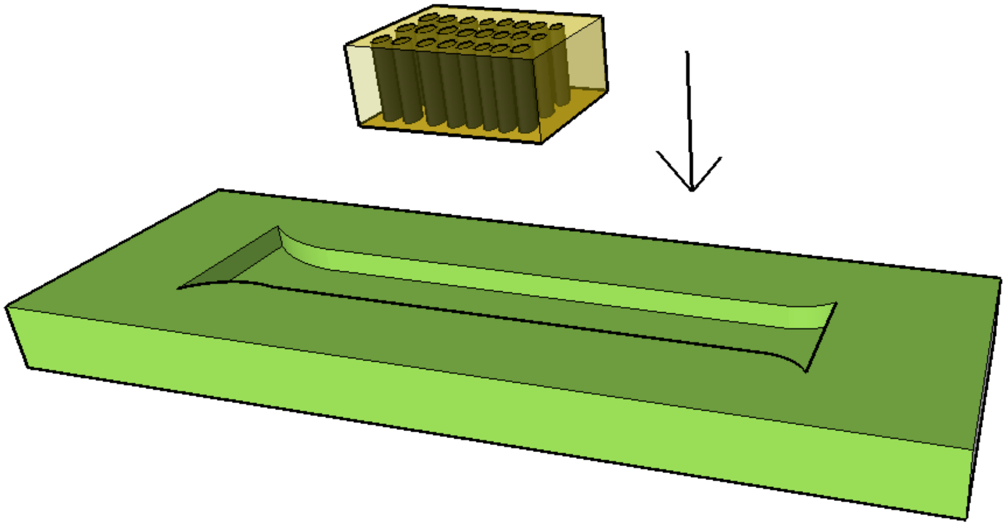

Figure 3.3 Representation of A- PNC Block Insertion into Dogbone Silicone Mold

This process was usually relatively straightforward compared with the very difficult PNC fabrication stage; however, some practical problems remained to be overcome in this instance also. Usually the molds could be easily ‘peeled’ off the newly cured sample following the cure; however, on some occasions, molds that had experienced heavy use would adhere to the sample and crack the dogbone as it was being removed from the mold, again rendering them unusable. This tended to occur only with older, and heavily reused molds; after this had happened several times, therefore, such molds were avoided to the extent possible. Additionally, this was particularly problematic during the creation of shear samples, which presented a sharp 90-degree angle to the flowing epoxy which almost invariably resulted in bubbles in the cured samples near the PNC-epoxy interface, especially at the bottom of the mold. It is not entirely clear why this occurred, as the bubbles were not visible when placing the samples into the oven prior to a cure, but always appeared afterward; however, it is thought to result from some interaction of the flow of the epoxy with the sharp PNC edge, and likely also reflected expansion of tiny air bubbles trapped in that region due to the heating. These bubbles had to be sanded and polished away before the shear samples could be used for testing.

Polishing (i.e. sanding) the samples was an important step that was required before the dogbone samples could be used for tensile testing. Upon removal from the molds, the dogbone samples were extremely uneven on all four sides: on top (where they tended to be extremely concave), bottom (often included some roughness) and the sides (which were usually ribbed due to the way the mold negative had been cut). The top and bottom had to be sanded differently than the sides due to the presence of the dogbone projections, and the sanding of these two pairs of sides will therefore be discussed separately.

The polishing of the dogbone top and bottom was relatively straightforward. A small quantity of Crystalbond material was heated on a hot plate and allowed to liquefy. It was then spread on top of a small aluminum block. The sample to be polished was then placed onto the top of the block using tweezers. Weights were placed on the sample, and the Crystalbond was allowed to dry and set, holding the dogbone sample in place. The aluminum block was then used to hold the sample over a spinning sanding wheel which was spun at 300 rpm using 1200 grit silicon carbide sandpaper. The sample was sanded by physically pressing the aluminum block (and the attached sample) against the sanding wheel. This would rapidly and evenly smooth down the top surface of the dogbone sample. The sample, now sanded ('polished') and its aluminum block would now be placed back on the hot plate, with the sample facing up. This melted the Crystalbond and allowed the sample to be picked up off the block and flipped over, so that now the bottom could be polished. This was done in an identical way to sanding the top surface of the sample, after which the sample was removed from the aluminum sanding block.

The polishing of the sample sides proved to be far more challenging. Because of the design of the projections of the tensile testing specimens, it was not possible to simply mount the samples on the sanding blocks and polish their sides in the same way as was done for the top and bottom of each sample. Several different methods of accomplishing the polishing of the sides were attempted. At first, hand sanding was used, but due to the great time demands of this technique, mechanized versions of side polishing were explored. The first idea was an attempt to use a felt bobbin (drill bit) attached to a drill press to sand the sample, which would be mounted on an x-y table; this had been suggested when advice on the problem was solicited from other researchers. The bobbin was dipped into a grit solution to allow for abrasion. However, it was found that the bobbin was not sufficiently abrasive to adequately polish the sample, even with the added grit; additionally, the diameter of the smallest bobbins available was still large enough that it would have been necessary to hand sand small regions in the corner of each sample even had the bobbin been abrasive enough to polish the rest of the sides. An attempt was made to affix sandpaper of a higher grit directly to the bobbin, but the aforementioned diameter problem was made worse by the attachment of the relatively thick sandpaper. Therefore, after a period of experimentation this felt bobbin approach was discarded. Several avenues of investigation into the use of a mill did not produce results when machining experts informed the experimenter that there was no suitable bit that could be placed in the mill that would accomplish the sanding as required without damaging the rest of the sample. A handheld Dremel was used in another attempt, with the sample again suspended on an x-y table, but this approach lacked a way of applying the necessary precision. Finally the optimal method was found to be use of a Dremel 438 ¼" 120 grit drum sander mounted on a mill, as this allowed precise control of the machining.

Speckling the samples- i.e., applying a fine pattern of dots to their surfaces in order to apply digital image correlation –also proved to be much more challenging than was originally anticipated by the experimenter.

As discussed earlier, numerous methods exist for speckling a sample; there is no single accepted technique for how to speckle a given sample, so several different methods were tried. Originally airbrushing was attempted, but extreme difficulty was encountered with this approach. Later this was determined to be due to damage to the airbrush being used, but as this was unknown at the time, several other methods were tried. First, an attempt was made to spray paint the samples directly from a spray paint can held at a distance; however, this was found to result in dots that were far too large for DIC when the samples speckled in this way were examined under a microscope. Next, printer toner was tried as a speckling agent; a printer cartridge was obtained and opened, and a straw used to blow the toner across the samples. This method produced very small dots when viewed under a microscope, but they both tended to clump together in unpredictable ways and, more importantly, did not adhere well to the samples surface, even when a base of wet paint was applied before the toner was blown across the surface. Therefore, this method also proved inadequate for the needs of this work. It was also suggested that the experimenter hit the toner cartridge against a table and try to pass the samples through the resulting cloud of toner. This was also tried; (perhaps needless to say) it did not work either, due to even more extreme clumping of the toner when examined under the microscope.

Finally it was attempted to experiment with the airbrush again. A new airbrush, a Badger 200G with gravity feed and a fine head, was obtained and the results proved to be far superior to those originally acquired with the older, damaged airbrush. This technique proved to yield dots that were small, adhered well to the white spray-painted sample surfaces (for contrast), and did not clump together; it was therefore used for the final speckling of all samples whose data are seen here.

First a coat of Rust-Oleum Flat White Spray Paint was sprayed over the sample in two quick passes over the sample with the spray paint can held at arm's length from the sample. The spray paint was allowed to dry for approximately 30 minutes. The Badger 200G airbrush was then connected to a Badger TC908 Aspire compressor and filled with Dr. Ph. Martin's Matte Black Star India Ink. The sample was held at arm's length from the airbrush and two-three quick bursts of black ink were applied, lasting approximately half a second each. The black speckles were allowed to dry for approximately one hour. The speckling process is shown in Figure 3.4, with a photograph of speckled and unspeckled specimens illustrated in Figure 3.5. Comparisons of successful speckling methods with the initial unsuccessful techniques are shown in Figure 3.6.

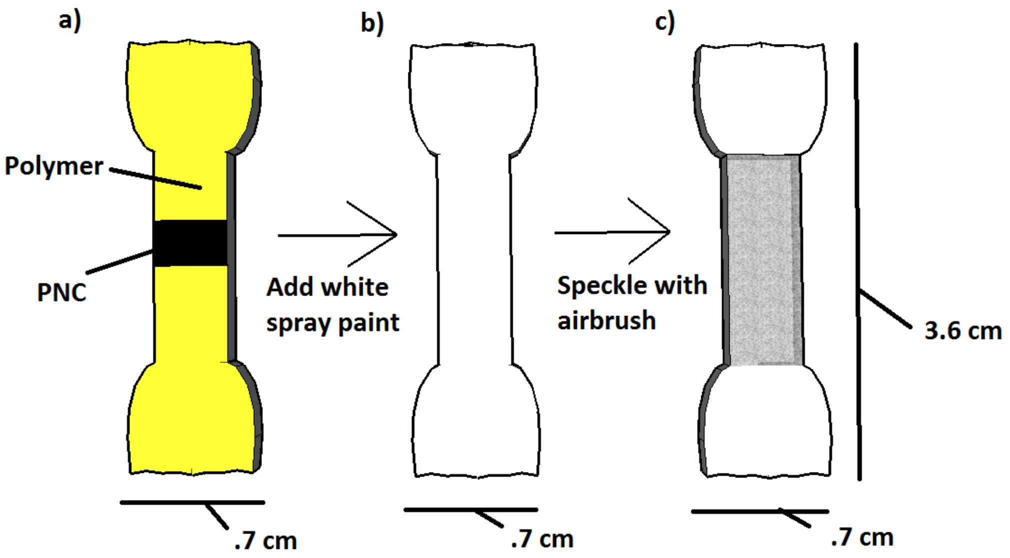

Figure 3.4 Speckling Process. a) Unspeckled sample. B) Spray-painted sample. C) Spray-painted and airbrushed sample.

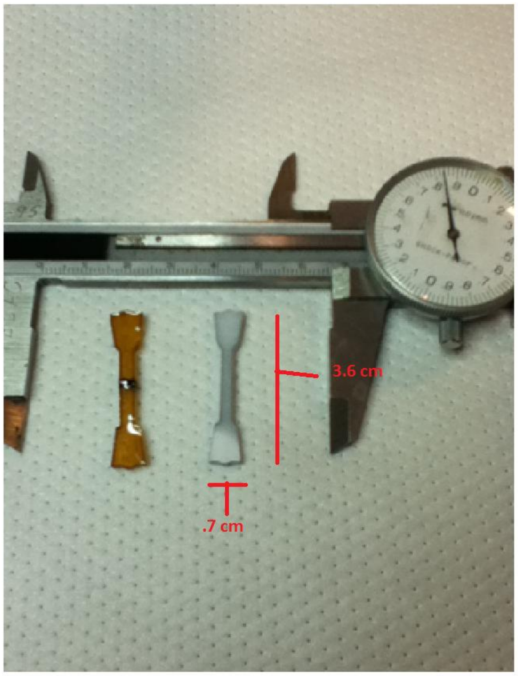

Figure 3.5 Speckled Sample (right) Compared to Unspeckled Sample (left).

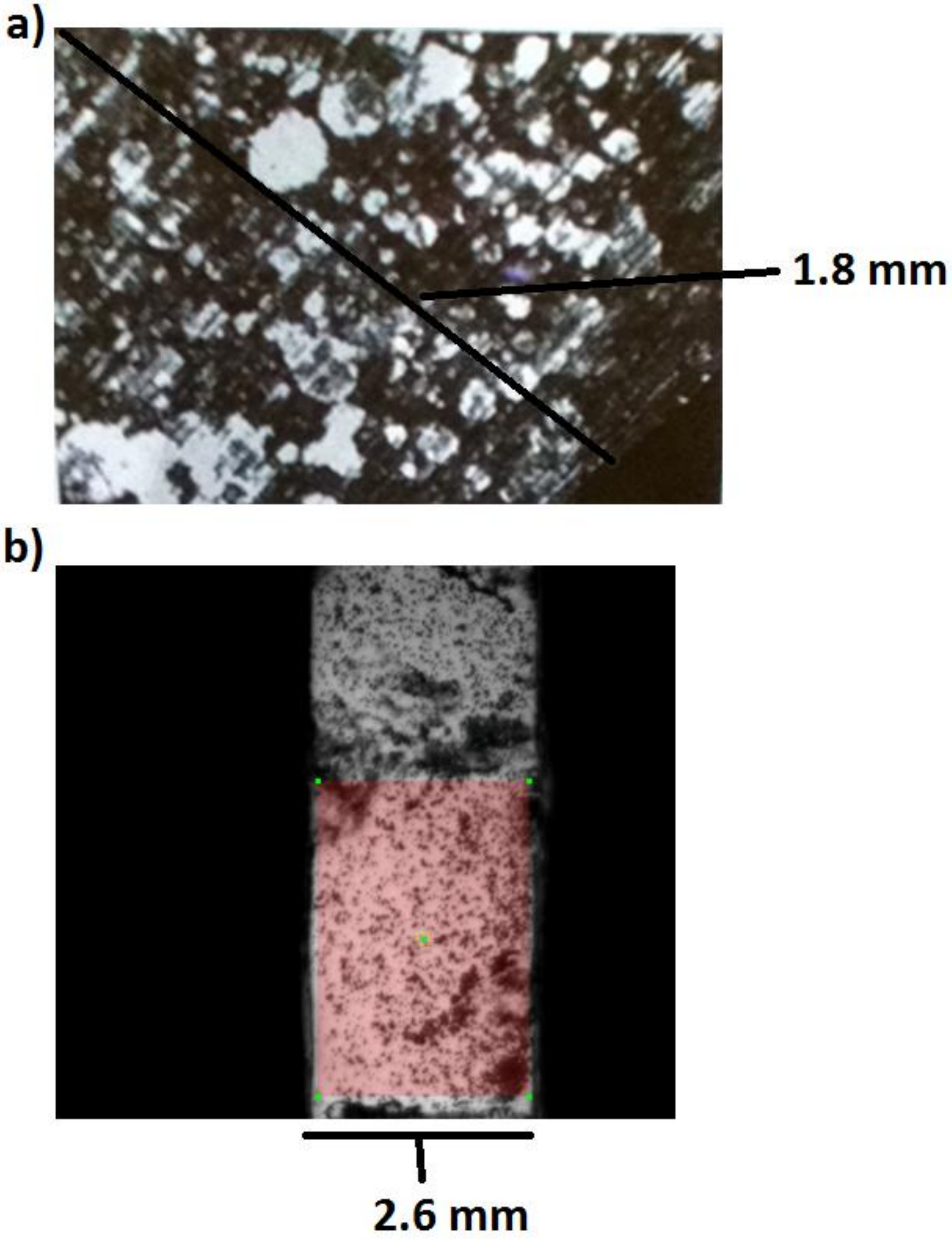

Figure 3.6 Comparison of Speckling Processes. a) Sample speckled with white spray paint on a black ink background. Note the large uneven clumps present in the spray paint speckles. b) Sample speckled with printer toner. Note the uneven clumping characteristic of this speckling material.

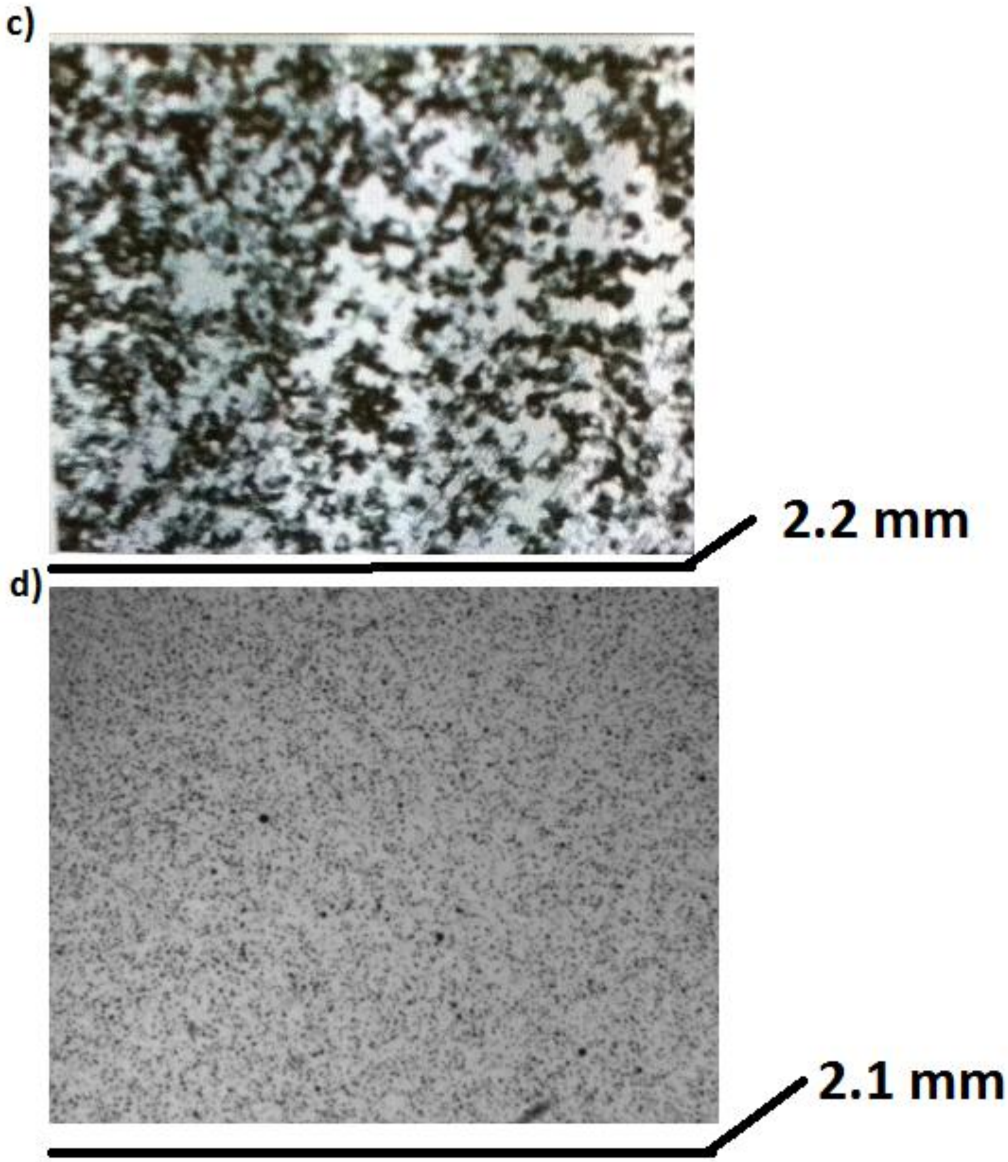

Figure 3.6 (continued) c) Sample speckled with an airbrush and an ink that tends to clump (Super Matte Black). Note the highly uneven speckle pattern. d) Sample speckled with the final combination of airbrush and ink. Note the small, nearly evenly spaced speckles near the limits of resolution.

Longitudinal tests were normal tensile tests performed with the CNTs mounted parallel to the major axis of the dogbone samples, while transverse modulus values were derived from testing PNC samples that were rotated 90 degrees into the testing plane (i.e. CNTs were perpendicular to the axis along which the force was being applied).

Shear testing was somewhat more complex. When a shear test was performed, the CNTs would be oriented at a 45 degree angle within the dogbone mold, and then tested in the same manner as the longitudinal and transverse samples. This positioning allowed for derivation of the constitutive relations by using the assumption of transverse isotropy and subsequently rotating the stresses and strains to determine the shear modulus necessary to produce the observed strain patterns.

3.2. Mechanical Testing

3.2.1 MIT Testing

Once the samples had been cured, polished, and speckled, the next step was to perform the actual tensile testing. These tests involved use of a Zwick Z-010 tensile testing machine; a Rettiga 1300 camera (later replaced by a higher resolution Point Grey digital camera); a Manfrotto aluminum tripod with a geared head; a fiber optic light box with dual light guide heads; a C-mount adapter and telephoto lens for the Rettiga camera, and a Navitar Zoom 6000 lens for the Point Grey; and a USB data acquisition (DAQ) system. Several software programs were used; Vic-2D 2009 (used primarily, and exclusively for final analysis and results shown here) along with HDPE, used for testing and noise examination, and VicSnap 2010, for controlling acquisition of images by the digital camera. All three of these products are made by Correlated Solutions, Inc., and were used for all DIC-related computer analysis. The software testXpert II, made by Zwick, was used to control the tensile testing machine.

The first step of running a test was to set up the camera and machine for testing. The Zwick machine was turned on using a large switch on its side; after this, the testXpert software could be started on an adjacent desktop computer. Once this was accomplished, the tripod was placed close to the machine's front (precise placement method will be discussed later) and the digital camera affixed to the tripod head using the quick-release foot that attached to the tripod head. The teleconverter and telephoto lens were also connected to the digital camera. The computer containing the Correlated software (Vic 2D, VicSnap, and HDPE) was mounted on a separate wheeled cart; this was plugged in and the computer turned on. Once the computer was on, the digital camera was attached to the computer using a 15-foot long FireWire cable, which both supplied power to the camera and also served to transfer the imaging data to the computer. The lightbox would then be placed on a cardboard support behind the Zwick machine and turned on. The USB cable from the Zwick machine's DAQ system was also connected to the computer containing VicSnap 2010 at this time. Proper lighting and alignment of the samples were vital for gathering good imaging data, as illustrated in Figure 3.7

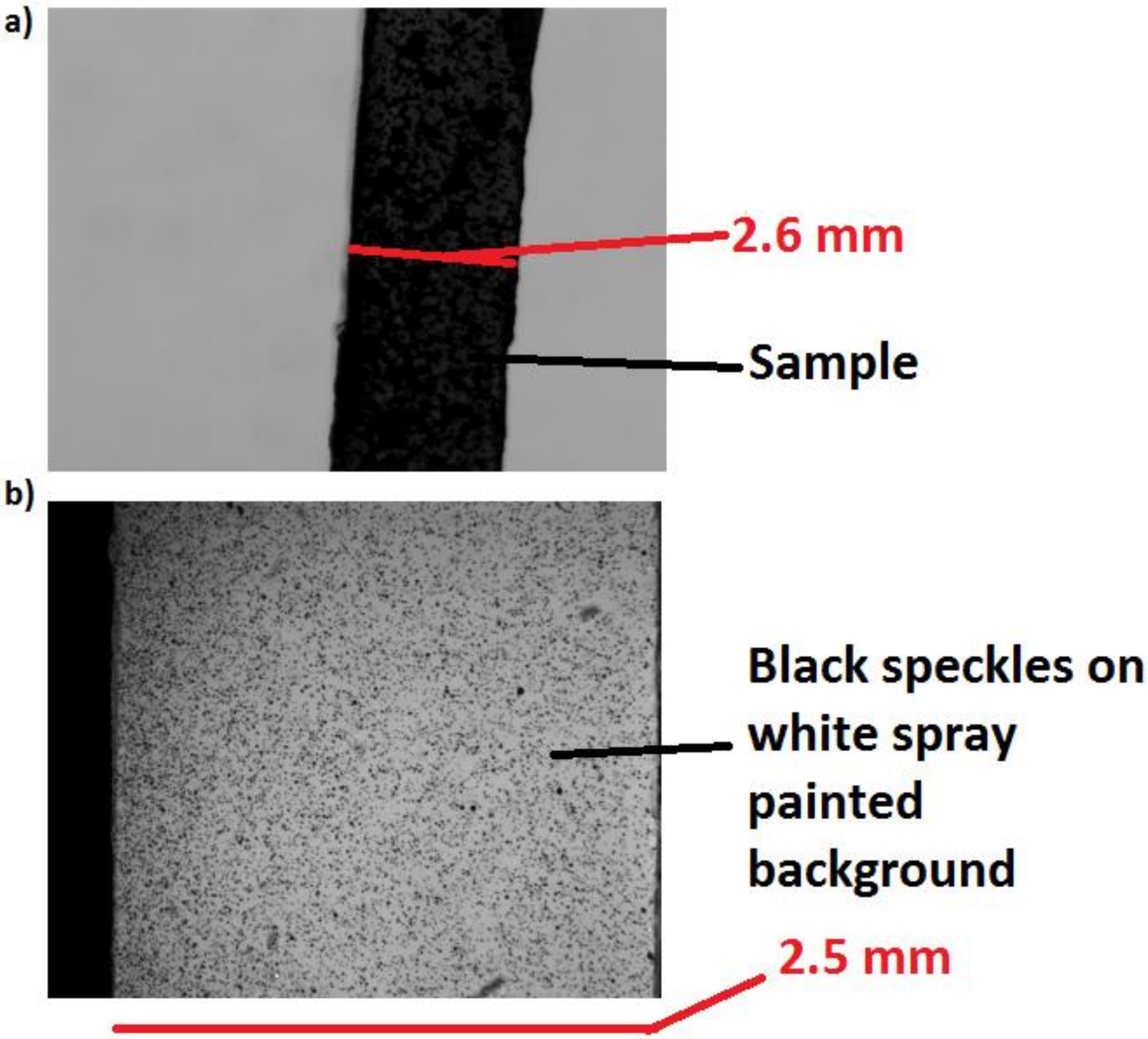

Figure 3.7 Importance of Lighting and Alignment. A) A very early test with poor lighting and alignment of sample. B) A later test with improved lighting ,reduced exposure time and precise alignment with tensile testing machine.

Once it was verified that the digital camera was producing good imaging data and the Zwick machine was on and connected to testXpert, a test was run to ensure that the DAQ system was functioning properly. Four channels of data are shown on the VicSnap input, three of which are blank and populated only by noise; it was ensured that the fourth channel showed a force reading corresponding with the output displayed on testXpert (i.e. that force data were being fed properly to VicSnap via the DAQ). This allowed for stamping of each individual image with force data rather than trying to manually align this data from the Zwick computer with the timestamps on the VicSnap images. Once this was accomplished, force data would automatically be read into a spreadsheet, with the force corresponding to each individual numbered imaged available for every image captured by VicSnap during a test. A photograph of the testing setup is shown in Figure 3.8.

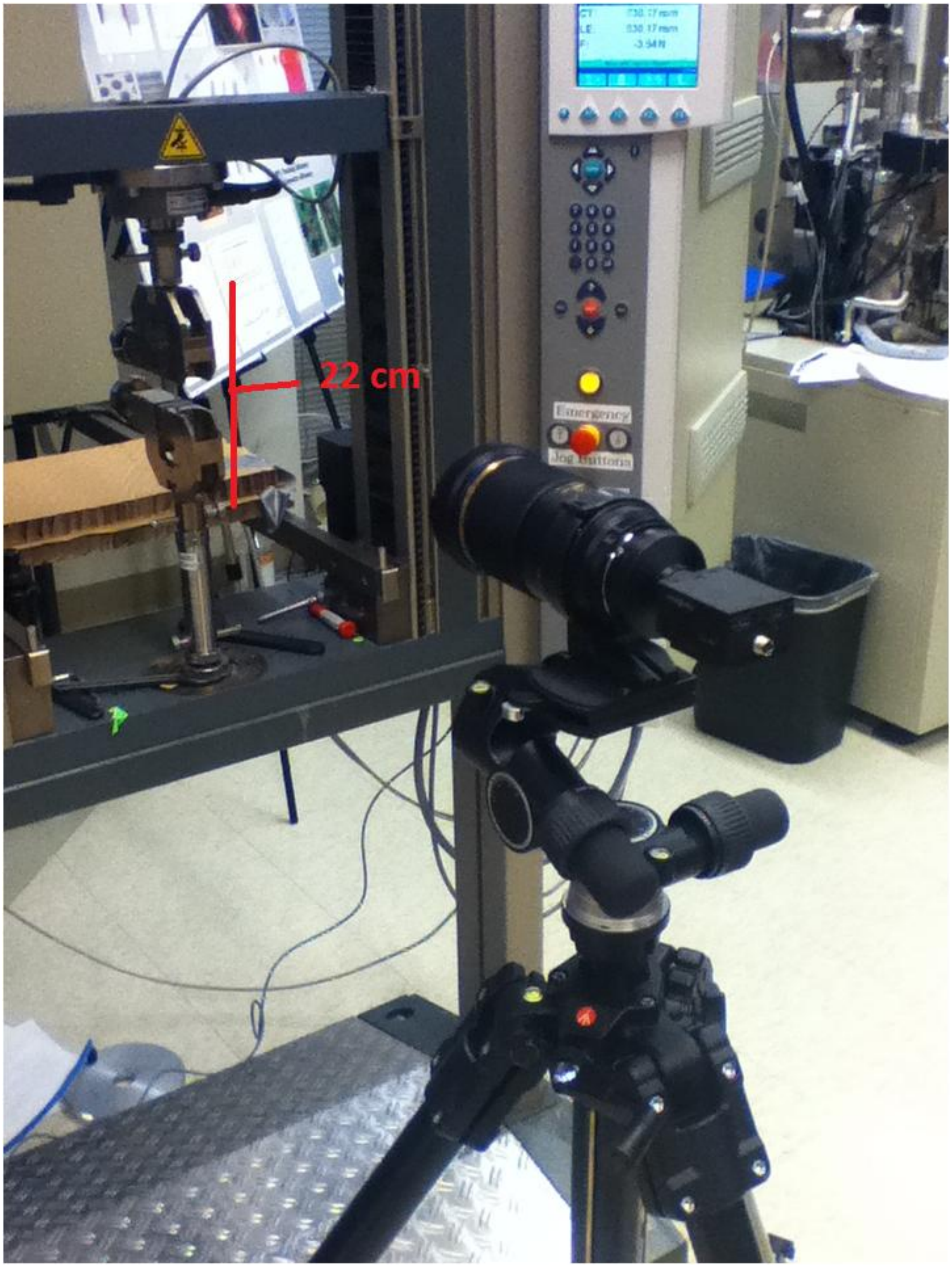

Figure 3.8 MIT 2-D Tensile Testing Setup. Tensile testing machine is on left with camera/tripod on right.

Next, the sample was loaded into the Zwick machine. This was done by unscrewing the clamps on the Zwick test grips (1 kN grips) and then retightening them. The sample was loaded into an approximately straight vertical position which would be adjusted subsequently. If the grips were not at the proper distance at the start of the test, which was almost invariably the case, they would be moved closer manually using testXpert's start position selection option until the grips were properly spaced to grip the two ends of the sample. Once the sample was approximately in position, the next step was to focus the camera.

This was done by first moving the camera approximately 23 inches from the grips (measured with a tape measure). This had been determined in previous tests to be the minimum distance at which the camera could focus. The camera would be aimed at the sample for use in the focus test. The camera focus would be manually moved all the way to the closest setting; if it were possible to move any closer (by fractions of an inch) and stay in focus, this was done by nudging the tripod forward so as to maintain the maximum possible resolution for a given test. Quality of focus was determined by a diagnostic tool available within VicSnap; it was possible for this tool to measure the quality of the focus using a sliding bar. Making this bar as high as possible was the method used to obtain the best possible focus for a given image. Once the proper focus and distance were obtained, the camera was leveled in two axes using a manual bubble level. This usually resulted in minor focus and aim adjustments that had to be made subsequently as this leveling would very slightly change the aimpoint of the camera.

Once the camera was leveled and focused on the specimen at the closest possible point, the specimen was then rotated to be in the most vertical alignment possible (i.e. exactly perpendicular to the ground). This was accomplished by aligning the line of pixels that represented the outer edge of the specimen on the VicSnap screen to be as close to the local vertical as possible (which could be seen as the edge of the VicSnap screen). The lightbox was then turned up to maximum and the light heads placed as close to the specimen as possible without obstructing the view of the digital camera. The exposure time of the camera was then turned down via VicSnap until no overexposed (red) areas were visible on the image; this generally occurred around a 5 ms exposure time, and in practice this was usually the exposure time used, with the camera f/stop placed on its fastest setting.

At this time, it was finally possible to begin the test. The Zwick machine was set via testXpert to apply a maximum of 25 N to the samples so as to avoid fracture. Once these parameters were verified to have been programmed into the Zwick via testXpert, the imaging sequence was prepared in VicSnap. The program was set to record 1 image per second for an unlimited period, until commanded by the user to stop. The tests were displacement controlled and proceeded at a rate of .2 mm/min, as it was found that at approximately this speed the 1 image per second guideline would capture pixel movement between images just above the noise floor (i.e. at slower rates of movement, the average feature movement in pixels per second was lower than the noise measured for stationary features; see section 4.2. Also as a practical matter at significantly slower test speeds the file sizes became exceedingly unwieldy for analysis unless a lower imaging rate was used). Imaging was then begun and immediately followed by the command via testXpert for the Zwick to start its testing cycle. Once the Zwick had loaded 25 N onto the sample, the test was stopped and the load slowly brought back down to the starting point. VicSnap imaging was ended after the load began to cycle back down. Once the test cycle was complete, the sample was removed from the grips, and either another sample would be loaded in the Zwick (only the vertical alignment of the sample required full repetition upon loading multiple samples; the focus, aim, etc. required only very minor adjustments) or the testing gear would be stowed and shut down.

3.2.2 NASA 3D Testing

Part of the cross collaboration with NASA involved the use of a Vic 3D system to study the accuracy and noise of the MIT 2D system. Results of this testing will be discussed later; here we will discuss the points of difference in test preparation and execution between Vic 2D and Vic 3D.

Vic 3D is a significantly more complex program to use than Vic 2D. Aside from the obvious complication of using two cameras, there is a sophisticated alignment algorithm that is necessary with Vic 3D that is not found with Vic 2D (Vic 2D is essentially a version of Vic 3D with some of the functions disabled; otherwise, the software works identically).

VicSnap is similar in that the same program supports 3D imaging, and some of the functions are simply disabled when using 2D mode.

The NASA Vic 3D system at Langley Research Center (LaRC) uses two Point Grey cameras mounted on an aluminum bar for spacing and a powered Questar tripod for control, along with a Tytron 250 tensile testing machine. The Questar tripod contained electronics that transferred the imaging signals from the cameras to the computer; it also received commands from the computer to move the cameras in two axes (vertical and horizontal) and to move the two cameras relative to each other along the bar. To initiate a test in Vic 3D, the Questar tripod was placed with its baseplate in contact with the table supporting the Tytron machine. However, prior to conducting a test, the machine had to undergo the calibration technique discussed. This Vic 3D calibration involved the use of a small glass plate with a number of dots placed on it in a grid pattern. The plate was black and had transparent spaces in it that served as the dots for this exercise; it was manufactured and provided by Correlated Solutions. The technique of calibration involved taking an image of the calibration plate, having the computer calculate where the dots were, and then moving the camera slightly in one of its axes and repeating this procedure. By comparing how far the actuators in the tripod moved the camera mounting with the shift of the dots, the computer was able to calculate a converged 3D solution for the relative location of the glass plate in space after 8-12 images. This 3D solution calibrated the spacing of the cameras relative to each other and allowed use of the now-calibrated Vic 3D system for three-dimensional DIC (provided the spacing of the cameras was not subsequently changed). The NASA Vic 3D system is shown in a photograph in Figure 3.9.

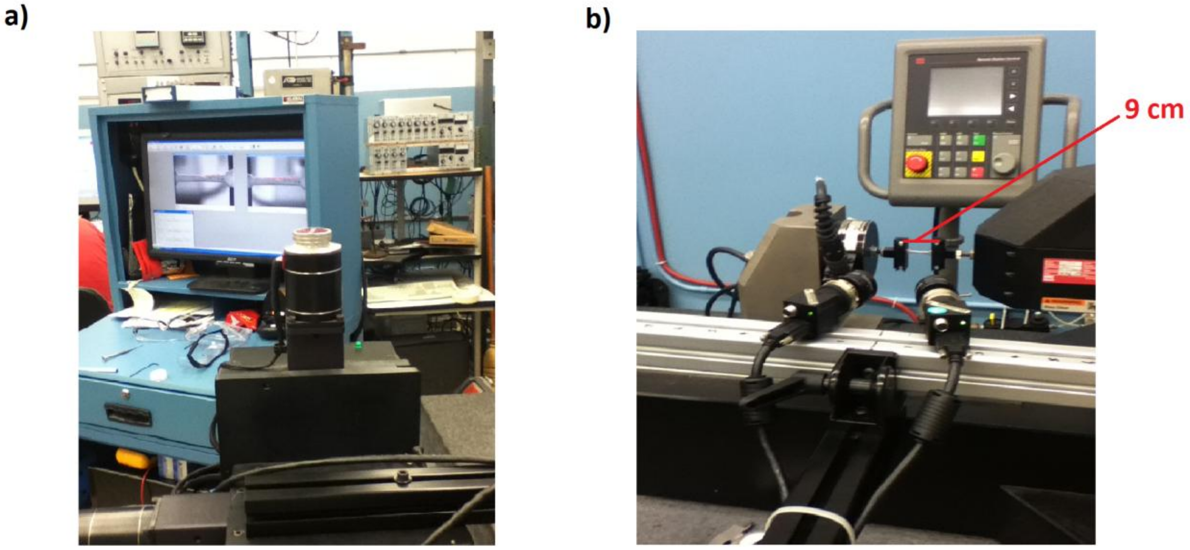

Figure 3.9 NASA Vic 3D System. A) Computer readout. B) Point Grey cameras on Questar tripod.

Next, the sample was loaded into the Tytron 250. Unlike the Zwick, this machine had an automatic routine that could be used to properly space the grips depending on the size of the sample; the grips were secured by the use of very small screws. A lightbox was not necessary for this apparatus; the tests were performed using ambient light. The Tytron was controlled via its own computer program using a test sequence programmed using identical parameters to those described for the Zwick machine. VicSnap was also used for control of the NASA Vic 3D system; a 1-second imaging interval was also used for the Vic

3D tests. The actual tests were performed in a nearly identical way to the Vic 2D test procedure discussed above; the imaging was begun immediately prior to the start of the test; once the Tytron machine reached the end of its load cycle; the imaging was ended and the machine allowed to bring the load back down before subsequent removal of the sample, and either loading of a new sample or shutdown of the test apparatus. Analysis of the Vic 3D tests differed slightly from the Vic 2D tests; this will be discussed in a later section.

3.2.3 Data Analysis and Reduction: Vic 2D

The majority of the post-test analysis work was done using Vic 2D, with the exceptions of the noise investigations (done using HDPE and detailed later) and the ‘quick-look’ NASA results using Vic 3D, also discussed later. After completion of a test, the imaging data was loaded into Vic 2D for analysis. This was done by clicking the “Speckle images” button on the Vic 2D menu screen. All the images from the test in question would then be selected from the appropriate folder and loaded. Next, the first image would be selected in the “AOI Editor” (Area of interest editor). The AOI editor allowed definition of the “area of interest”- that is, the area of the image that actually recorded the sample rather than the blank sides of the image. This permitted Vic 2D to perform its analysis only on those areas of the image that were known to contain data (i.e. the speckle pattern on the lit sample) and vastly cut processing time by ignoring blank spaces. This was done by dragging a rectangle using the AOI Editor tool over the part of the image that contained the sample. This rectangle would have to be slightly larger than the actual size of the sample since during the analysis a slightly smaller area than the desired AOI was actually measured (one of Vic 2D's many software bugs). Next, processing parameters were set using the Start Analysis tool, selected via a green arrow on top of the Vic 2D screen.

There are several parameters involved in Vic 2D processing but the most important ones are the subset and step size. Details on these parameters can be found in[44], written by the creators of Vic 2D. Essentially, a subset size represents the size of a region, in pixels, over which Vic 2D will attempt to smooth out strain variations (or more precisely, it will smooth out displacement field variations, which will then producing resultingly smoother strain fields). For example, for a subset size of 20, Vic 2D will smooth out the displacement field by looking at regions approximately 20 pixels across as moving as a single unit. Larger subset sizes had the advantage of greater accuracy in that they were able to average displacement over larger regions and thus eliminate some noise (as will be discussed in detail later). However, larger subset size selections suffer from two major disadvantages: processing time and loss of spatial resolution.

Inherent in the increased advantage in average displacement accuracy gained by the use of the larger subset is a corresponding loss in spatial resolution, since real displacement variations from place to place will be smoothed out over much larger regions. For example, if a CNT region for a given sample is only 25 pixels across linearly, but a subset size of 150 is being used, the real spatial variation in displacement across the CNT region vs. the neat epoxy regions of a sample will be averaged out and lost, simply changing the average strain measurement over a much larger region (which will now also be inaccurate, since the lower strain in CNT region will be averaged across a large region of pure epoxy region and lower the average strain measured across those areas). In addition, processing time rises dramatically with increased subset size, by approximately the square of the subset size selected[44]; this could lead to nontrivial (overnight) processing times for larger subset sizes (~100 pixels or larger). However, disadvantages were encountered in the use of smaller subset sizes also; the use of a subset that was too small would result in two few speckles being present in a region of the selected subset size, resulting in far greater noise in the data (as will be discussed in detail below) and the possible identification of false discrete spatial regions of displacement introduced by the selection of this small subset size. After much experimentation and the noise analysis that will be detailed later, a subset size of 101 was finally settled upon for the analyses shown here (101 was selected because it was found that Vic 2D would often crash if the subset size number did not end in 1; this was another of its many bugs).

In order to calculate strain from the displacement field, it was necessary to perform another calculation. This made use of the “strain filter”, which is essentially a subset for strain. The subset size discussed above is used for the displacement field calculation; the strain filter then performs basically the same calculation but using the displacement data as an input rather than the original image. This behaved in the same way as the subset size, i.e. a larger strain filter would average the strain over larger regions and get better numerical accuracy for the average strain in a given region, but spatial resolution would suffer and vice versa. The reason why both strain filter and subset size are important to set independently was that the subset is acting directly on the actual image data, whereas the strain filter is operating only on the displacement field calculated by Vic using the subset. Therefore, strain filters that were very large compared to the subset size (Correlated's rule of thumb for "very large" was a strain filter 2/3 the size of the subset size) were not useful because they averaged the strain over such a large region that spatial accuracy was lost. For maximum numerical accuracy, this 2/3 rule of thumb for sizing the strain filter was used, and thus the subset size became the only completely independent variable.

The step size was basically the distance that the algorithm would travel between different subset or strain filter locations. For example, a step size of 3 would mean that the center of each new subset region would start 3 pixels away from the center of the previous location (see[44] for more detail). The step was set to 5 for both strain and displacement, which was the default; as with the subset, it was found that Vic 2D contained a bug that would usually cause the program to crash if the step did not end in a 5, and 15 was considered an unusually high number for the step size. The effect of using different subset sizes and strain filters on the same image is shown in detail in Figure 3.10.

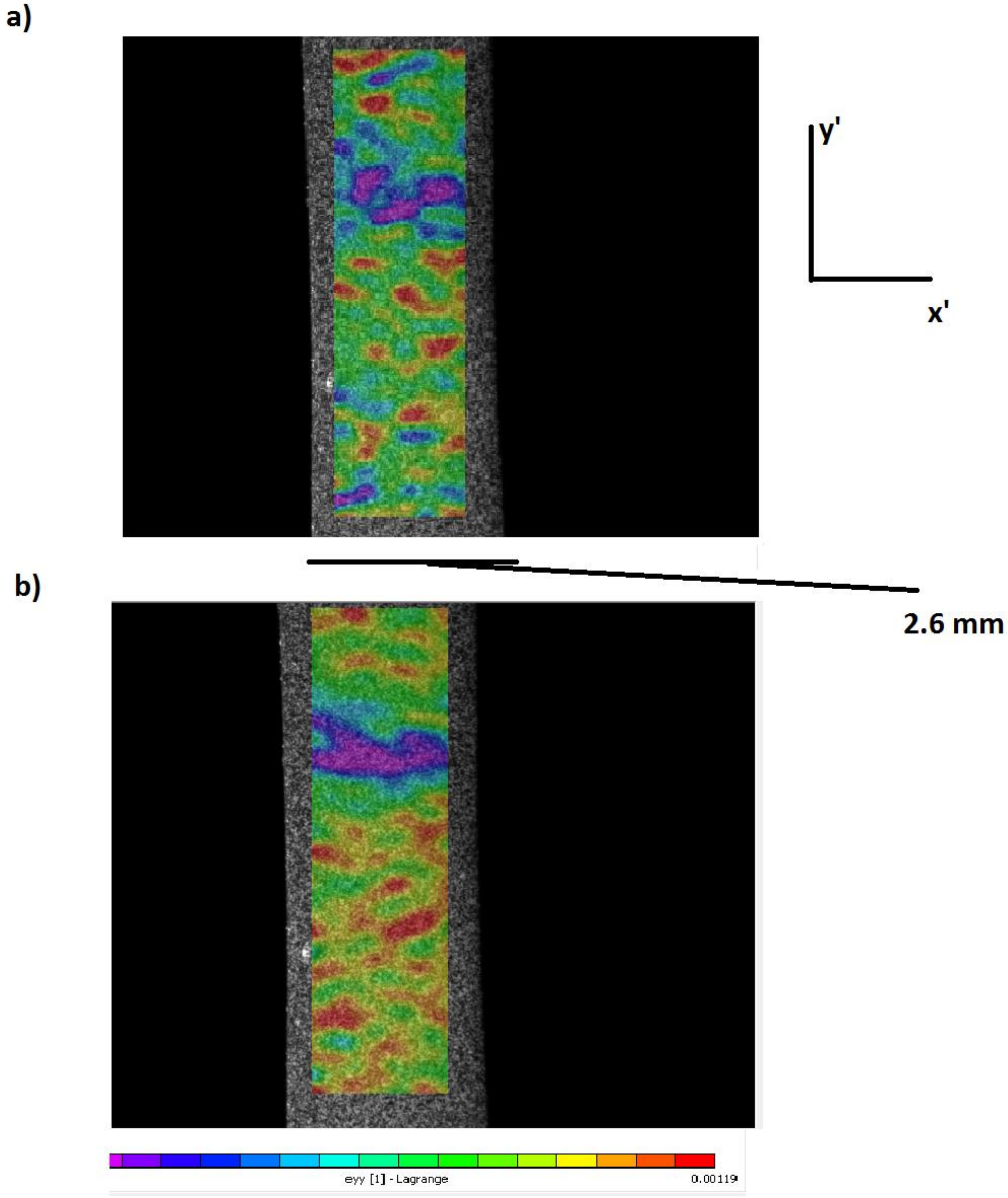

Figure 3.10 Effect of Different Processing Techniques on DIC Results. a) Results of using a subset that is much too small, 21 pixels. b) Appropriately sized subset (101 pixels) but strain filter is too small (15 pixels). All subfigures of Figure 16 use the same strain scaling, shown at the bottom of each subfigure. ε_{yy} shown.

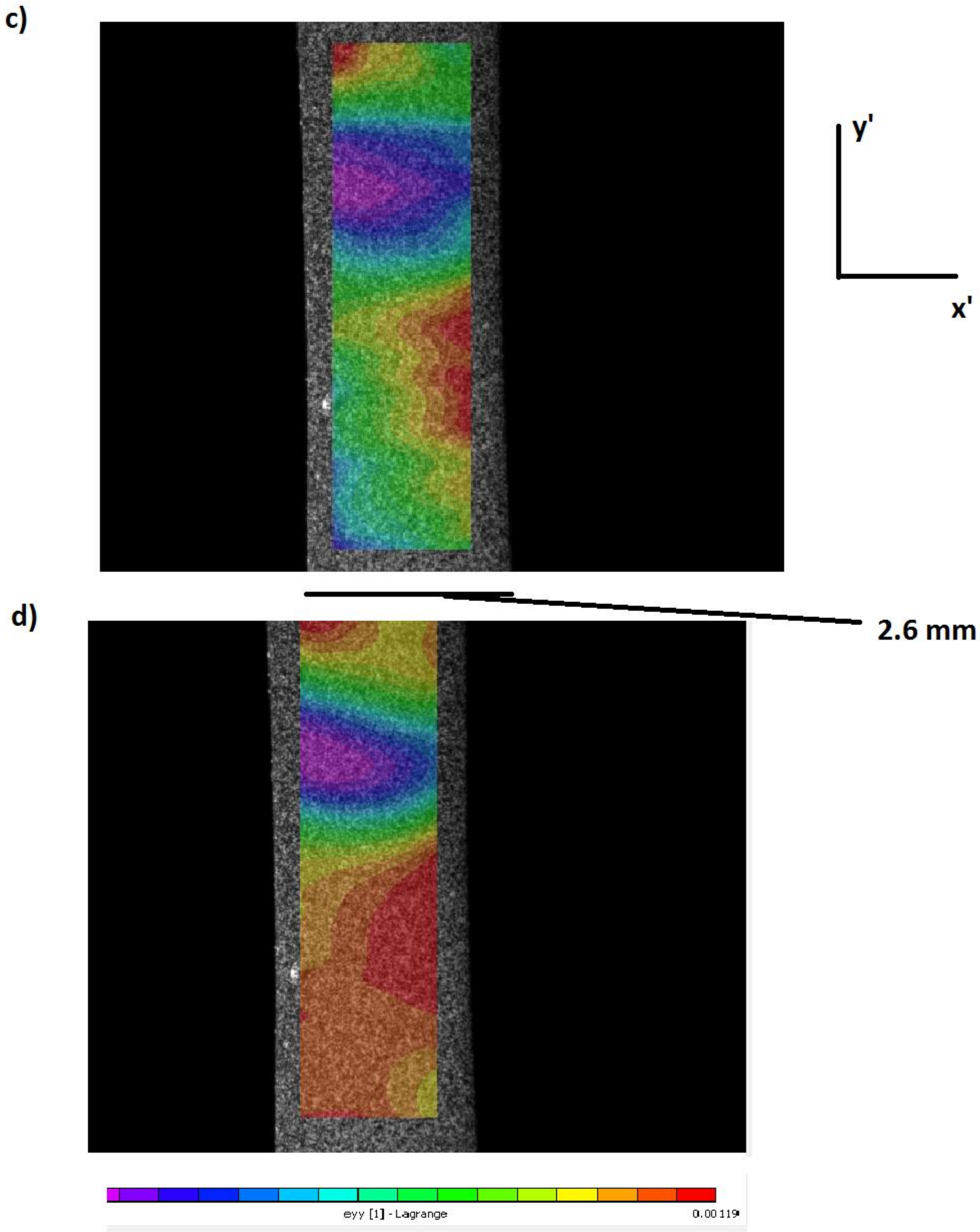

Figure 3.10 (continued) Effect of Different Processing Techniques on DIC Results. c) Results of using an inappropriately large strain filter, 55 pixels. b) Subset too large (151 pixels) with strain filter too small (15 pixels). ε_{yy} shown.

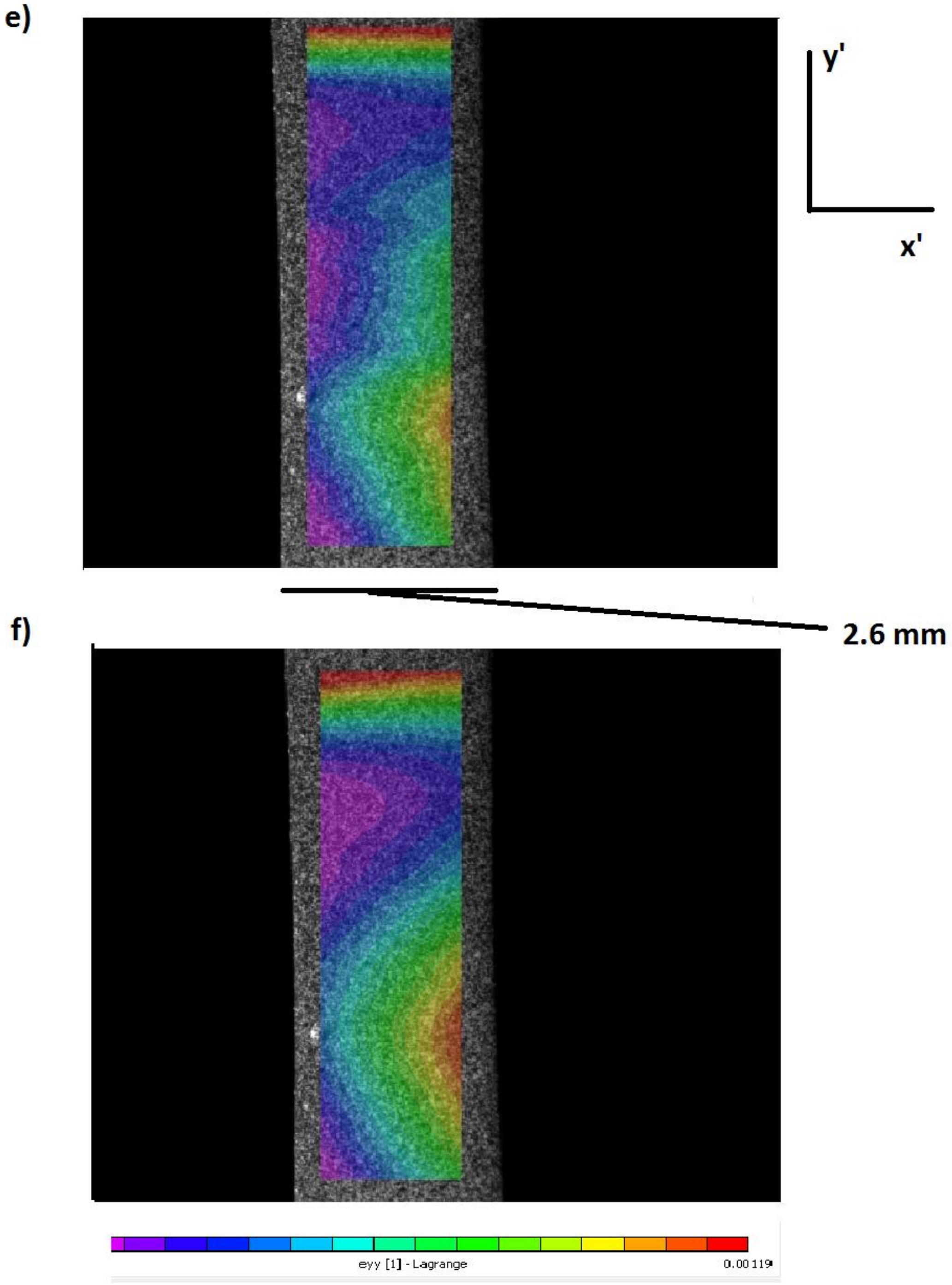

Figure 3.10 (continued) Effect of Different Processing Techniques on DIC Results. e) Use of a strain filter that is much too large (75 pixels). f) Use of a large strain filter coupled with the use of a Box filter instead of a Lagrange filter. ε_{yy} shown.

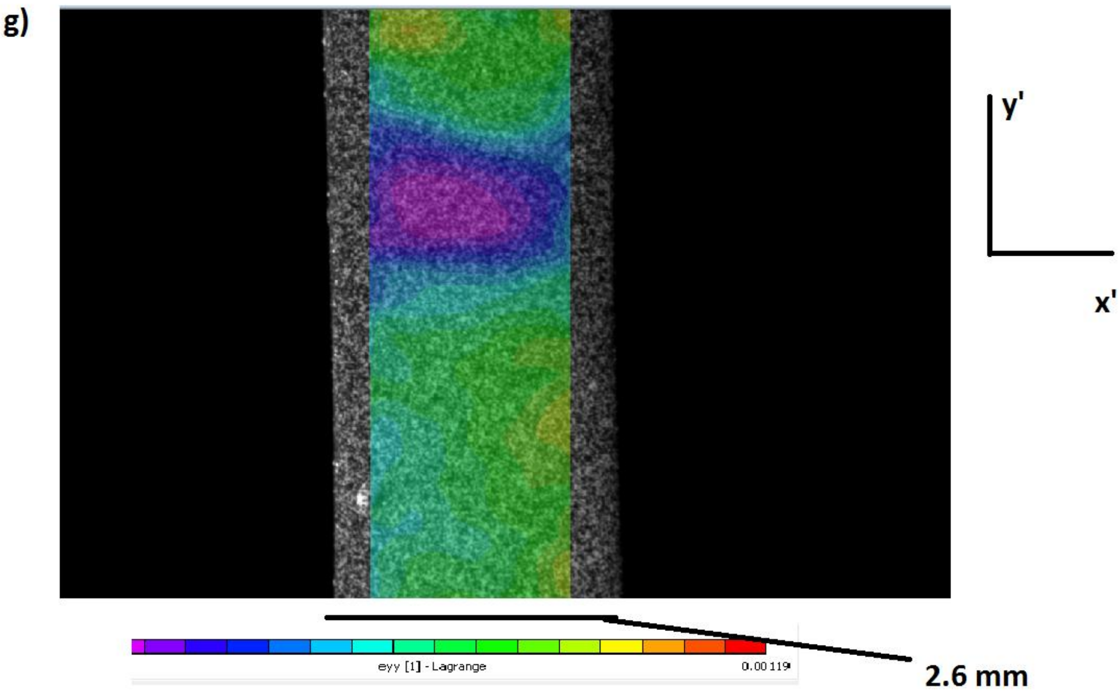

Figure 3.10 (continued) Effect of Different Processing Techniques on DIC Results.. g) Properly processed image, subset size 101, strain filter size 35. ε_{yy} shown.

Once these parameters were programmed into Vic 2D, the analysis was begun; this was an automated process. The wait time for the completion of the processing was, depending on parameters and the exact number of images captured for the analysis, usually between approximately 60 minutes and 12 hours (for extremely large subsets and long tests. Those analyses whose results are shown here, with the final subset size of 31, were much closer to the short end of that range).

Once the analysis was complete, the data could be examined in a variety of different ways. By clicking on the “Data” tab after the analysis it was possible to see a complete readout of all DIC-derived data for each image in an interface similar to that which was presented for the selection of AOIs in the AOI editor. By clicking on each image, a spatial representation of strain was shown; by right clicking on this image it was possible to display different kinds of data as a colored graphical overlay (i.e. ε_{xx}, ε_{yy}, u, v, etc.). Desired data could also be extracted in numerical form by using the Inspector tools. By dragging a rectangle (or other desired shape) over the area that numerical data was desired from, this same set of parameters could be extracted from all the images analyzed using the "extract" tool (selected by a small "x" on the Inspector menu) and read out to a spreadsheet. This allowed strain values averaged over the areas of interest (i.e. CNT region or neat epoxy) to be read out numerically for all image files, so that they could be used in the later analysis.

Once Vic 2D's data was read out to a spreadsheet as described above, the numerical analysis of the data could begin. First the imaging data was matched with the force data which was available from the spreadsheet of force data for each image created by the DAQ system from the Zwick machine outputs, as discussed above. The modulus was calculated in several steps. First, the area was calculated by using a caliper on the samples' central straight area and averaging the measured width at three locations along the dogbone. The stress was then found for each timestep by dividing the force output from the DAQ by the area of the sample. The strain for each timestep was output from Vic-2D directly. The modulus in the appropriate axis was then found by dividing the stress by the strain and averaging over all the timesteps (excluding the first 10 seconds; these were dropped due to noise issues, as will be discussed in more detail later). The Poisson's ratio appropriate to the particular measurements was found by dividing the strain measured by Vic 2D in the orthogonal axes in question and averaging over the same set of timesteps.

The shear modulus was derived via the use of CNTs aligned at 45 degrees and shear rotations. Using the convention shown in Figure 1.3 (reproduced here for convenience) and calling the testing axes, illustrated in Figure 3.11, y' (load direction), x' (direction perpendicular to load in image plane) and z' (out of image plane), the stress in each laminate axis was first calculated as:

(for σ_1 applied only, $\theta=45^o$)

$$\sigma_{yy} = \cos^2\theta\ \sigma_{y'} \tag{3.1}$$

$$\sigma_{xx} = \sin^2\theta\ \sigma_{y'} \tag{3.2}$$

$$\sigma_{xy} = -\sin\theta\ \cos\theta\ \sigma_{y'} \tag{3.3}$$

These stress values were found using the σ_1 output from the Zwick machine. Next, laminate strain was found as (in tensor notation):

$$\varepsilon_{yy} = \cos^2\theta\ \varepsilon_{y'} + \sin^2\theta\ \varepsilon_{x'} + 2\sin\theta\ \cos\theta\ \varepsilon_{y'x'} \tag{3.4}$$

$$\varepsilon_{xx} = \sin^2\theta\ \varepsilon_{y'} + \cos^2\theta\ \varepsilon_{x'} - 2\sin\theta\ \cos\theta\ \varepsilon_{y'x'} \tag{3.5}$$

$$\varepsilon_{xy} = -\sin\theta\cos\theta\ \varepsilon_{y'} + \sin\theta\ \cos\theta\ \varepsilon_{x'} + (\cos^2\theta - \sin^2\theta)\varepsilon_{y'x'} \tag{3.6}$$

where $\varepsilon_{y'}$, $\varepsilon_{x'}$, and $\varepsilon_{y'x'}$ are outputs from Vic, and

$$G_{xy} = \sigma_{xy}/2\varepsilon_{xy}. \tag{3.7}$$

in this, the principal material axes.

More information on the constitutive relations leading to the derivation of the shear modulus equation can be found in Jones.[59]

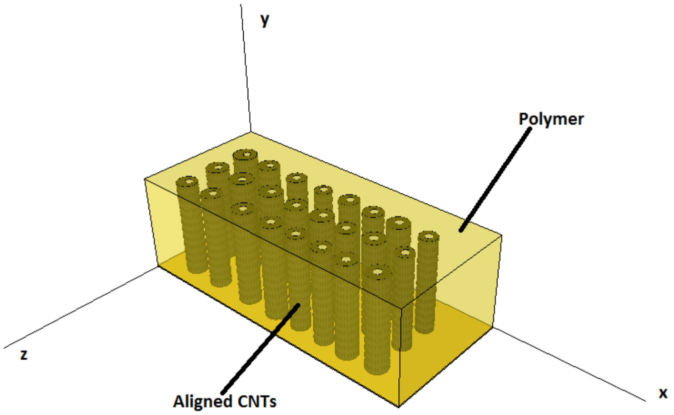

Figure 1.3 Schematic of Aligned CNT PNC (A-PNC) Material

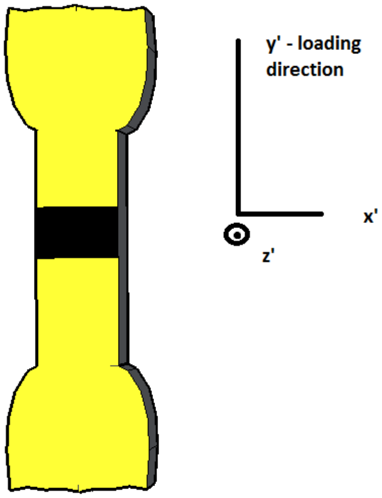

Figure 3.11 Testing Axes Nomenclature Referred to in Text

Due to the noise issues being experienced with the MIT setup, part of the cross-collaboration with NASA pursued as part of the NSTRF collaboration involved retesting some of the same samples tested at MIT in order to determine how close the measurements were with NASA's completely independent Vic 3D system of much higher resolution. As the name suggests, Vic 3D is a version of Vic 2D that uses two cameras in order to add the dimension towards and away from the camera (Z) to the strain measurements. The software is also manufactured by Correlated Solutions (Vic 2D is in fact essentially a downgraded version of Vic 3D with the 3D functions locked out). The NASA setup was described in detail above. Once the imaging and test were completed, the data was read out to a spreadsheet and the analysis conducted in essentially an identical way; the NASA system also outputted force directly to the computer with a similar data acquisition system for use in modulus calculation. As will be shown in detail below, the modulus results obtained using the NASA system were quite similar to the MIT results.

Chapter 4

Results

4.1 Discussion of Optical Strain Results

Results are presented in Figure 4.1 and Table 4.1. A linear trend in modulus is observed in Table 4.1 and Figure 4.1 with increasing volume fraction of A-PNCs from the baseline epoxy, for longitudinal, transverse, and shear specimens, and axes as shown in Figure 1.3. As has been previously discussed[11,12], the A-PNC modulus is far from that predicted in a simple rule of mixtures analysis for collimated CNTs in a matrix: *e.g.,* for 20% volume fraction aligned CNTs with a MWNT fiber modulus of 0.5 TPa, the composite modulus is expected to be ~60 GPa, rather than ~6 GPa measured here. Similar behavior has been observed in testing via nano-indentation for the A-PNC system studied here.[11] Further, it has been demonstrated that CNT waviness has a strong effect on the longitudinal (CNTs axis) and transverse A-PNCs modulus via finite element modeling.[13-15] Waviness reduces the reinforcing effect of the fibers in the fiber direction, and increases it in the transverse direction, in the same way that misaligned fibers reduce stiffness and other properties. Poisson's ratio (see Table 4.1 and Figure 4.1) is also measured by comparing the strain in the axis perpendicular to that along which the force is being applied in a given test, utilizing the strain fields calculated by Vic-2D. Results are consistent with reciprocity within the achievable accuracy of the test and there is no discernible trend with volume fraction over the range considered. It is interesting to note that the A-PNCs are effectively isotropic until Vf>~10%, underscoring the importance of CNT waviness on the stiffness tensor. Manufacturer's reported value for RTM6 isotropic modulus is 2890 MPa, Poisson's ratio v=0.38.[60]

Table 4.1 Constitutive Relations of A-CNT PNCs as a Function of Volume Fraction, Where c_{ijkl} is the Stiffness Tensor in $\sigma_{ij} = c_{ijkl}\varepsilon_{kl}$, Table made by Daniel Handlin and Itai Stein.

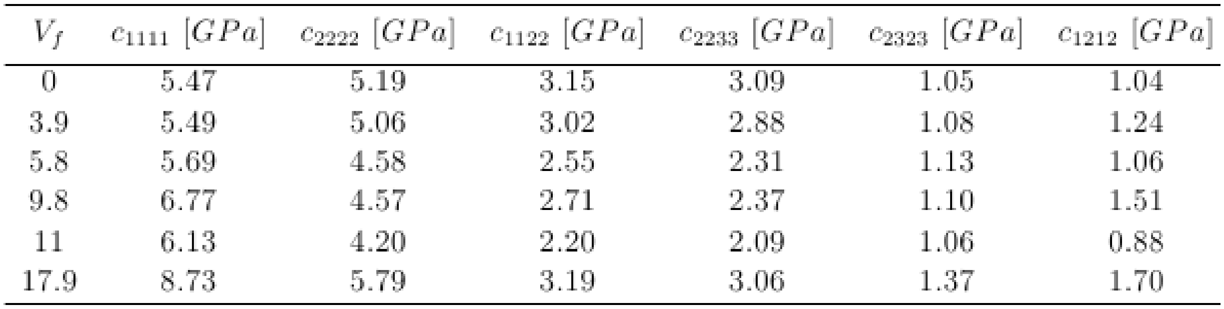

V_f	c_{1111} $[GPa]$	c_{2222} $[GPa]$	c_{1122} $[GPa]$	c_{2233} $[GPa]$	c_{2323} $[GPa]$	c_{1212} $[GPa]$
0	5.47	5.19	3.15	3.09	1.05	1.04
3.9	5.49	5.06	3.02	2.88	1.08	1.24
5.8	5.69	4.58	2.55	2.31	1.13	1.06
9.8	6.77	4.57	2.71	2.37	1.10	1.51
11	6.13	4.20	2.20	2.09	1.06	0.88
17.9	8.73	5.79	3.19	3.06	1.37	1.70

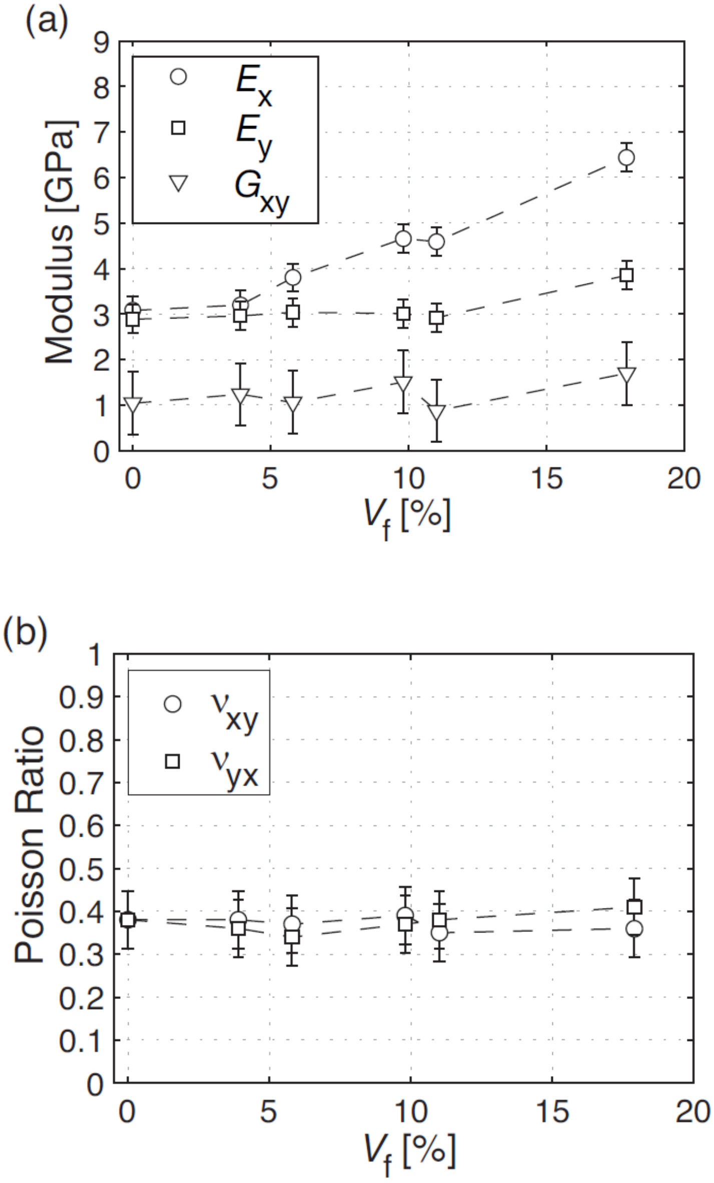

Figure 4.1 Constitutive Relations of A-CNT PNCs as a Function of Volume Fraction. a) Elastic modulus of A-PNCs as a function of aligned CNT volume fraction. b) Poisson's ratios as a function of aligned CNT volume fraction. Figure made by Daniel Handlin and Itai Stein.

The current work underscores structure-property relations and understanding of the A-PNC materials. The results are consistent with what would be expected from standard micromechanics (if fiber waviness is accounted for) and the morphology of the fibers. As the volume fraction of the fibers is increased, the morphology remains the same (i.e. the waviness does not decrease), resulting in an increase in the measured longitudinal elastic modulus, noting that the stiffness increase is less than would be predicted by the rule of mixtures due primarily to the CNT waviness.[11] As can be seen, there is also an increase in observed transverse modulus, which would not be predicted from rule of mixtures but which is consistent with the presence of the CNT waviness. Shear modulus is minimally affected even at high packing fractions, as also would be expected.

One of the key implications of these results is its relevance to the question of load transfer in "fuzzy-fiber" composites.[13] Previous work modeling the transfer of load from the matrix to the fuzzy fibers[17] has assumed that the presence of CNTs in the matrix induces a large change in the elastic properties of the matrix. However, this work shows that there is a significantly smaller change in the elastic properties of the matrix than had been assumed in the extant work. This suggests that the addition of CNTs to the matrix does not have nearly as drastic an effect as had been assumed on the way that loads are transferred from the matrix to the fibers in such composites.

Recent work by our group has shown that[18] the strength of the fuzzy fiber/matrix interface is increased by approximately a factor of 2 over the unmodified matrix material. The work herein suggests that this strength increase is not caused by an increase in stiffness of the CNTs in the polymer matrix, but reflects the CNTs actually increasing the strength of the interface itself. This study also suggests that the interfacial shear strength of the fuzzy fiber composites (~1% Vf) reported in that work cannot be accounted for by large modifications to the matrix elasticity.

4.2 Noise Investigation

One of the key investigations undertaken with respect to generating a better understanding of the test environment and the achievable accuracy was a characterization of the level of noise in the images. Specifically, the intent was to determine the noise level in the images independent of confounding factors such as speckling patterns, lighting, and especially vibration. This last was especially challenging due to the fact that the testing apparatus was located on the fifth floor of a building with a great deal of other research equipment that led to noticeable vibrations at very high magnifications.

Since the purpose of these tests was to measure the maximum achievable accuracy with the equipment itself independently of these confounding factors to the greatest extent possible, it was decided to set them up differently from the standard tensile tests. For the noise characterization tests, the testing apparatus was moved to a room in the basement of the same building (in order to avoid vibration) and the samples held in a vise. Test setup was otherwise identical to standard tensile testing. The sample was held motionless in the vise and imaged with the Point Grey cameras for a period of 50 seconds. The images from these sessions were subsequently downloaded for analysis in Vic 2D and analyzed in manner identical to that of the standard tests. A selection of data from the noise tests is shown in Figure 4.2.

Four free parameters were taken in the noise study; the speckle pattern size (two different kinds of speckle patterns applied with different airbrush heads), use or non-use of a teleconverter lens, the exposure time, and the subset size, a Vic 2D parameter governing how much the strain field data are spatially smoothed across the sample. Each of these were varied across samples held in the vise. The standard deviation of the strain measured over the 50 second period for a nonmoving image was ~ 60 microstrain in a stationary, nonvibrating setup with optimal lighting and speckle pattern; variation of subset size with these parameters held fixed is shown in Figure 4.2. As can be seen, use of higher subset sizes significantly reduced noise in the strain calculations, although there was of course a corresponding drop in achievable spatial resolution. The variation of pixel position with time was also tracked to establish the vibratory environment in the testing area; an example of this form of data collection is also shown in Figure 4.2.

In addition, tests were undertaken using a very-high-magnification Questar QMC1027 long-distance microscope for imaging; however, the vibration meant that the these magnifications were not feasible due to excessive noise and jitter in these images; it also rendered the speckles impractically large for the fields of view that could be imaged with the Questar.

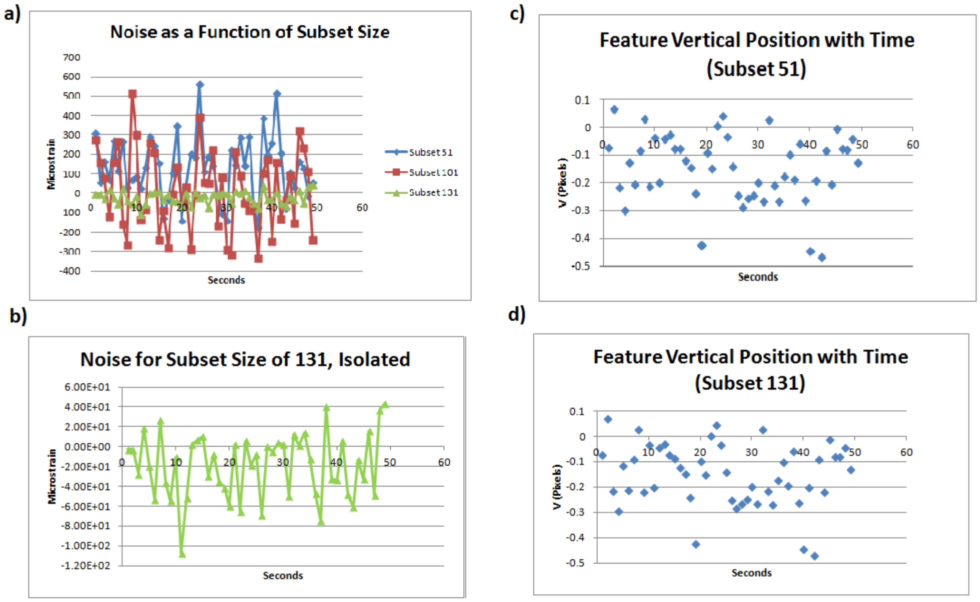

Figure 4.2. Selected Noise Investigation Results. a) Effect of changing subset sizes on noise scatter over time. b) Isolated noise distribution for a subset size of 131 pixels. c) Movement of vertical pixel position (as opposed to strain field) measured for a subset of 51 pixels. d) Vertical pixel movement measured for a larger subset of 131 pixels. Note c and d) are nearly, though not totally identical; a much greater difference in noise is seen after the strain calculation (a and b) rather than only after the displacement calculation (c and d).

4.3 Morphology Characterization

The samples have also been characterized to establish morphology. At NASA LaRC a very high-resolution SEM was used to investigate wetting of the CNTs; those samples examined were determined, via inspection of the SEM images, to be completely wetted in the CNT region as compared to other PNC specimens (not part of this study) which had visually obvious regions of voids and other non-wetted areas; a selection of these is shown in Figure 4.3. This imaging was supplemented via an investigation of the samples using Micro-CT (X-ray microtomography) techniques. The primary purpose of Micro-CT inspection was to search for voids or resin-rich areas in the samples- either of which could have major effects on measured sample modulus- as well to examine the shape of the samples to establish the cross-section and its uniformity and act as a general quality check to ensure good samples.

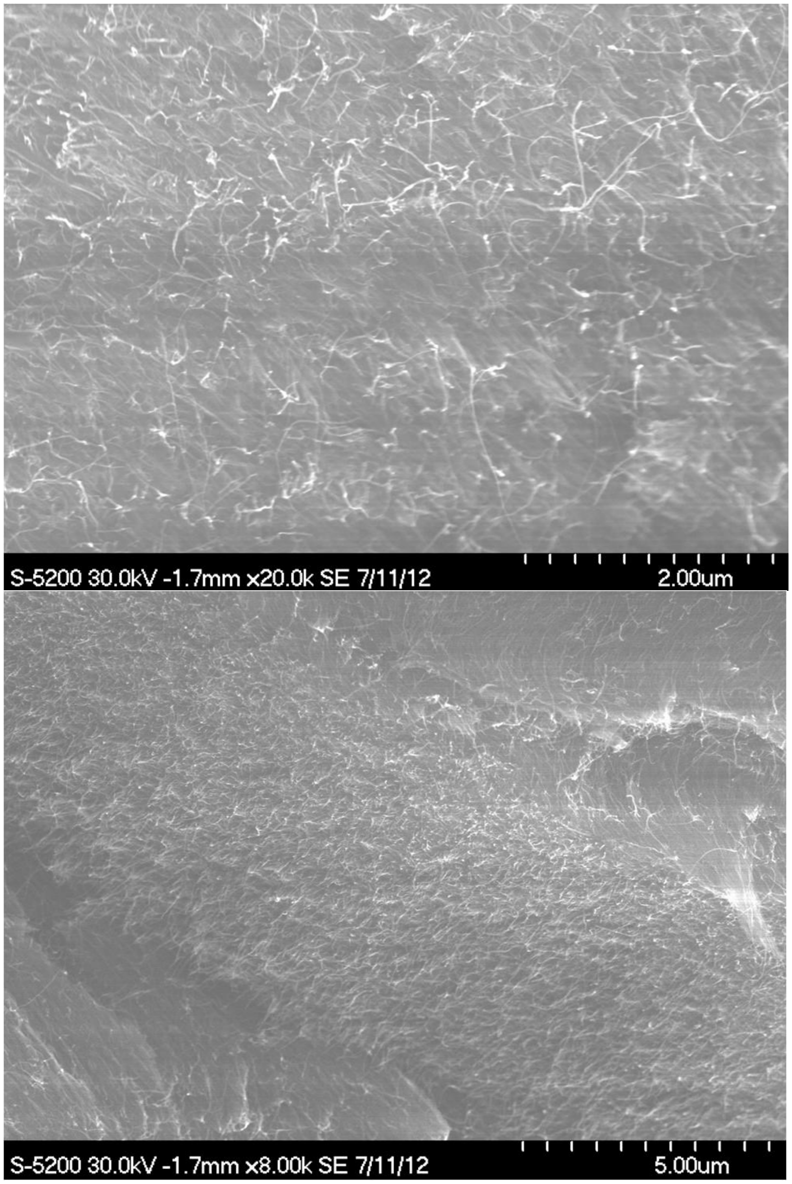

Figure 4.3 SEM Images of Fractured Aligned PNC taken at NASA. 10.7% Vf, longitudinally aligned fracture surface in epoxy resin.

The Vic 3D data were analyzed almost identically to the Vic 2D images. In the Vic 3D case, each camera produced a separate set of images, which ordinarily were used for a single calculation including a z component of the strain field. In this case, each camera's images were downloaded and analyzed separately within Vic 2D; the resulting modulus values, calculated in the same way as for the Vic-2D data described above, were then averaged together for each camera to arrive at the final values. The main goal of the Vic 3D testing was to show that the data yielded by testing with the MIT apparatus were within the error bars of the NASA measurement, in order to quantify the effect of the noise on the measurements of the sample taken at MIT. As can be seen, differences in the sample moduli measured between NASA and MIT were minimal. Comparison data are shown in Figure 4.4.

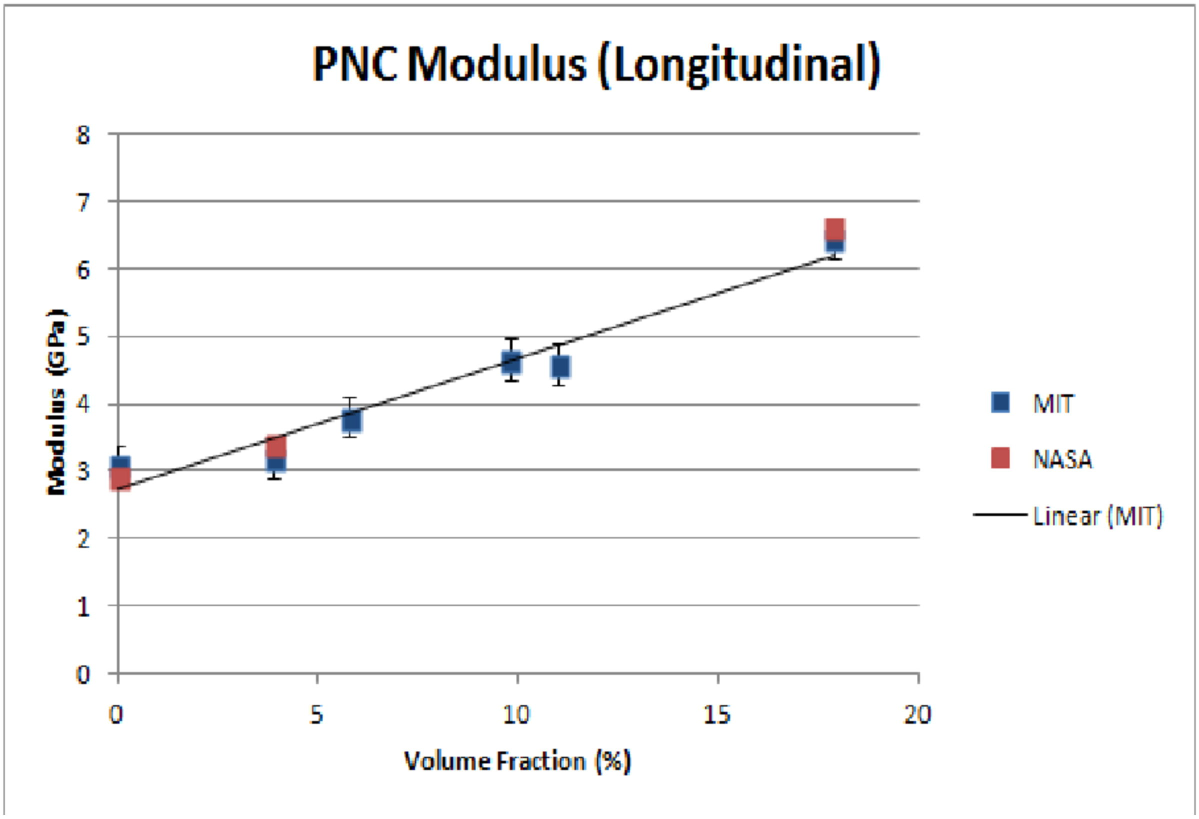

Figure 4.4 NASA Vic-3D Retests of Samples

4.4 Conclusions And Recommendations

Controlled nanoscale morphology in polymer nanocomposites can provide several advantages in advanced composites. Despite their potential structural and multifunctional applications, there is not a complete characterization of their mechanical properties. The current work is the first to provide measurements of the linear elasticity tensor for A-PNCs providing a basis for further constitutive model development. Tensile testing was performed to measure the elastic properties in all three dimensions of the composite constitutive relations. A linear trend in modulus is observed as a function of CNT volume fraction. CNT waviness is identified as a limiting factor on CNT reinforcement in composites, as expected from previous experimental work.

Tensile testing has been performed on both longitudinally and transversely aligned polymer nanocomposite specimens to measure the elastic properties in those axes, as well as on samples prepared for measurement of shear modulus. A linear trend in modulus is observed in each axis as a function of CNT volume fraction, although and there is very little effect of CNT reinforcement on transverse or shear modulus and both Poisson's ratios. The magnitude of the aligned CNT reinforcement is far below that calculated using collimated-fiber rule-of-mixtures due to the waviness of the CNTs, in line with both finite element predictions[13-15] and prior work on axial modulus measurements using nanoindentation.[11]

Funding

This work was supported by Boeing, EADS, Embraer, Lockheed Martin, Saab AB, Composite Systems Technology, Hexcel, and TohoTenax through MIT's Nano-Engineered Composite aerospace STructures (NECST) Consortium and in part by the U.S. Army Research Office under contract W911NF-07-D-0004 and W911NF-13-D-0001. It is also supported by NASA Space Technology Research Fellowship Grant #NNX11AN79H. This work made use of the Shared Experimental Facilities supported in part by the MRSEC Program of the National Science Foundation under award number DMR-0819762 and was carried out in part through the use of MIT's Microsystems Technology Laboratories, and Harvard's Center for Nanoscale Systems.

References

1. Wardle, B.L., Saito, D.S., Garcia, E.J., Hart, A.J. & Guzman de Villoria, R. Fabrication and Characterization of Ultra-High Volume Fraction Aligned Carbon-Nanotube-Polymer Composites. *Advanced Materials* **20**, 2008, pp. 2707-2714.
2. Ajayan, P.M., Tour, J.M. Materials Science: Nanotube Composites. *Nature*, **447**, 2007, pp. ` 1066-68.
3. Thostenson E.T., Li, C.Y. & Chou, T.W., Nanocomposites in Context. *Composites Science and Technology* **65**, 2005, pp.3-4.
4. Krishnan, A. Dujardin, E. Ebbesen, T.W. Yianilos, P.N.. & M.M. J. Treacy. Young's Modulus of Single-Walled Nanotubes. *Physical Review B* **58**, 1998, pp. 14013-19.
5. Wong, E.W., Sheehan, P.E., & C.M. Lieber. Nanobeam Mechanics: Elasticity, Strength, and Toughness of Nanorods and Nanotubes. *Science* **277**, 1997, pp. 1971-1975.
6. Li, C.Y. & T.W. Chou. Elastic Properties of Single-Walled Carbon Nanotubes in Transverse Directions. *Physical Review B* **84**, 2004, pp. 121-23.
7. Lu, J.P. Elastic Properties of Carbon Nanotubes and Nanoropes. *Physical Review Letters* **79**, 1997, pp. 1297–1300.
8. Srivastava, D., Wei, C., & K. Cho. Nanomechanics of Carbon Nanotubes and Composites. *Applied Mechanics Reviews*, **56,** 2003, pp. 215-230.
9. Allaouia, A., Baia, S., Cheng, H., & J.B. Bai, Mechanical and Electrical Properties of a MWNT/Epoxy Composite. *Composites Science And Technology* **62**, 2002, pp. 1993-8.
10. Ogasawara, T., Ishida, Y., Ishikawa, T., & R. Yokota, Characterization of Multi-Walled Carbon Nanotube/Phenylethynyl Terminated Polyimide Composites. *Composites Part A: Applied Science and Manufacturing*. **35**, 2004, pp. 67-74.
11. Cebeci, H., Guzman de Villoria, R., Hart, J., & B. L. Wardle, Multifunctional Properties of High Volume Fraction Aligned Carbon Nanotube Polymer Composites with Controlled Morphology. *Composites Science and Technology*. **69**, 2009, pp. 2649-2656.
12. Handlin, D., Guzman de Villoria, R., Chan, S., Takahaski, K., Cebeci, H., Williams, M., Parsons, E., Socrate, S., & B. Wardle. Elastic Properties of Aligned Carbon Nanotube Polymer Nanocomposites with Controlled Morphology. 53rd AIAA Structures, Structural Dynamics, and Materials (SDM) Conference. Honolulu, HI, April 23- 26, 2012.
13. Fisher, F.T., Bradshaw, R.D. & Brinson, L.C. Effects of Nanotube Waviness on the Modulus of Nanotube-Reinforced Polymers. *Applied Physics Letters* **80**, 2002, pp. 4647-4649.

14. Fisher, F.T., Bradshaw, R.D. & Brinson, L.C. Fiber Waviness in Nanotube-Reinforced Polymer Composites--I: Modulus Predictions Using Effective Nanotube Properties. *Composites Science and Technology* **63**, 2003, pp. 1689-1703.
15. Bradshaw, R.D., Fisher, F.T. & Brinson, L.C. Fiber Waviness in Nanotube-Reinforced Polymer Composites--II: Modeling Via Numerical Approximation of the Dilute Strain Concentration Tensor. *Composites Science and Technology* **63**, 2003, pp. 1705-1722
16. Wicks, S.S., Guzmán de Villoria, R., & B.L. Wardle, "Interlaminar and Intralaminar Reinforcement of Composite Laminates with Aligned Carbon Nanotubes", *Composites Science and Technology* **70**, 2010, pp. 20–28.
17. Ray, M.C., Guzman de Villoria, R., & B. L. Wardle. Load Transfer Analysis in Short Carbon Fibers with Radially-Aligned Carbon Nanotubes Embedded in a Polymer Matrix. *Journal of Advanced Materials* **41**, 4, 2009, pp. 82-94.
18. Lachman, N., Wiesel, E., Guzmán de Villoria, R., Wardle, B.L., & H. D. Wagner, Interfacial Load Transfer in Carbon Nanotube/Ceramic Microfiber Hybrid Composites. *Composites Science and Technology* **72**, 12, 2012, pp. 1416-1422.
19. Sumio I. Helical Microtubles of Graphitic Carbon. *Nature*, **354**, 1991, pp. 56-58.
20. Kilfrost Prepares for Winter Season. Aviation Today, 2010 <http://www.aviationtoday.com/regions/usa/Kilfrost-Prepares-for-Winter-Season_71496.html#.UVrkfhPD9Ms>
21. Patel-Predd, P. Carbon Nanotube Wiring Gets Real, IEEE Spectrum, 2008 <http://spectrum.ieee.org/semiconductors/materials/carbonnanotube-wiring-gets-real>
22. Zubrin, Robert. *Entering Space*. Tarcher: New York. 2000.
23. Yudasaka, M., Komatsu, T., Ichihashi, T., Iijima, S. Single-wall Carbon Nanotube Formation by Laser Ablation Using Double-Targets of Carbon and Metal. *Chemical Physics Letters*, **278**, 1–3, 24 October 1997, pp. 102–106.
24. Kumar, M., Ando., Y. Chemical Vapor Deposition of Carbon Nanotubes: A Review on Growth Mechanism and Mass Production. *Journal of Nanoscience and Nanotechnology* **10**, 2010, pp. 3739–3758.
25. Salvetat, J., Kulik, A., Bonard, J., Briggs, G., Stockli, T., & K Metenier. Elastic Modulus of Ordered and Disordered Multiwalled Carbon Nanotubes. *Advanced Materials*, **11**, 2, 1999, pp. 161-5.
26. Popov, M., Kyotani, M., Nemanich, R., & Y. Koga. Superhard Phase Composed of Single-Wall Carbon Nanotubes. *Physical Review B* **65,** 3, 2002, 033408.
27. Filleter, T., Bernal, R., Li, S., & H. Espinosa. Ultrahigh Strength and Stiffness in Cross-Linked Hierarchical Carbon Nanotube Bundles. *Advanced Materials* **23,** 25, 2011, pp. 2855-60.
28. Jensen, K., Mickelson, W, Kis, A, & A. Zettl. Buckling and Kinking Force Measurements on Individual Multiwalled Carbon Nanotubes. *Physical Review B*, **76** , 19, 2007, 195436.
29. Yang, Y.H. Radial Elasticity of Single-Walled Carbon Nanotube Measured by Atomic Force Microscopy . Applied Physics Letters **98**, 2011, 041901.
30. Pop, E., Mann, D., Wang, Q., Goodson, K. & H. Dai. Thermal Conductance of an Individual Single-Wall Carbon Nanotube Above Room Temperature. *Nano Letters* **6**, 1, 2005, pp. 96–100.
31. Berber, S., Kwon, Y.K. & Tomanek, D. Unusually High Thermal Conductivity of

Carbon Nanotubes. *Physical Review Letters***, 84**, 20 , 2000, pp. 4613–4616.

32. Hone, J., Whitney, M., Piskoti, C. & A. Zettl. Thermal Conductivity of Single-walled Carbon Nanotubes. *Physical Review B***, 59**, 4, 1999, pp. R2514–R2516.
33. Sinha, S., Barjami, S., Iannacchione, G., Schwab, A., Muench, G. Off-Axis Thermal Properties of Carbon Nanotube Films. *Journal of Nanoparticle Research* **7,** 6, 2005, pp.651-7.
34. Sanders, R. Physicists Build World's Smallest Motor Using Nanotubes and Etched Silicon. UC Berkeley,2003. <http://www.berkeley.edu/news/media/releases/2003/07/23_motor.shtml 2003.>
35. Naraghi, M., Filleter, T., Moravsky, A., Locascio, M., Loutfy, R., & H. Espinosa. A Multiscale Study of High Performance Double-Walled Nanotube−Polymer Fibers. *ACS Nano* **4**, 11, 2010, pp. 6463–6476.
36. Hussain, F, Hojjati, M., , Okamoto, M., & R. Gorga, Polymer-Matrix Nanocomposites, Processing, Manufacturing, and Application: An Overview. *Journal of Composite Materials*, **40**, 17, 2006, pp. 1511-75.
37. Gorga, R.E. & Cohen, R.E. Toughness Enhancements in Poly(methyl methacrylate) by Addition of Oriented Multiwall Carbon Nanotube. *Journal of Polymer Science, Part B: Polymer Physics,* **42**, 14 ,2004, pp. 2690–2702.
38. Sennett, M., Welsh, E., Wright, J.B., Li, W.Z., Wen, J.G. & Ren, J.F. Dispersion and Alignment of Carbon Nanotubes in Polycarbonate, *Applied Physics A: Materials Science & Processing,* **76**,1, 2003, pp. 111–113.
39. Andrews, R. & Weisenberger, M.C. . Carbon Nanotube Polymer Composites, *Current Opinion In Solid State & Materials Science*, **8**, 1, 2004, pp. 31–37.
40. Harris, P.J.F. *Carbon Nanotubes and Related Structures*, Cambridge University Press: Cambridge, UK, 1999.
41. Schadler, L.S., Giannaris, S.C. & Ajayan, P.M. Load Transfer in Carbon Nanotube Epoxy Composites, *Applied Physics Letters*, **73**, 26 , 1998, pp. 3842–3844.
42. Lau, K.T., Sankar, J., & Hui, D. Enhancement of the Mechanical Strength of Polymer-based Composites Using Carbon Nanotubes, in *Nanoengineering of Structural, Functional, and Smart Materials*, Schulz, M.J., Kelker, A.D. & Sunderasen, M.J. (eds.), CRC Taylor & Francis: USA, Chapter 14, 2006.
43. Han, J., Anantram, M.P., Jaffe, R.L., Kong, J. & Dai, H. Observation and Modeling of Single Wall Carbon Nanotube Bend Junctions. *Physical Review B*, **57**,1998, 14983.
44. Schreier, H., Orteu, J., & M. A. Sutton, *Image Correlation for Shape, Motion and Deformation Measurements Basic Concepts,Theory and Applications.* Springer: New York. 2009.
45. Sutton, M., Mingqi, C.,Peters, W., Chao, Y., & S., McNeill, Application of an Optimized Digital Correlation Method to Planar Deformation Analysis. *Image and Vision Computing*, **4**, 3, 1986, pp. 143–150
46. Crammond, G. Speckle Pattern Characterisation for High Resolution Digital Image Correlation. University of Southampton, September 8, 2011 <http://www.southampton.ac.uk/damtol/images/George%20Crammond%20ISEV%202011.pdf>
47. Reu P. & B. Hansche. Digital Image Correlation Combined with Electronic

Speckle Pattern Interferometery for 3D Deformation Measurement in Small Samples. 2006 SEM Annual Conference & Exposition on Experimental and Applied Mechanics. 2006.

48. Vic-3D 2010 Testing Guide. Correlated Solutions. <http://correlatedsolutions.com/support/index.php?_m=downloads&_a=downloadfile&downloaditemid=1>
49. McNeill, S. Digital Image Correlation. University of South Carolina. 2006. < http://www.me.sc.edu/fs/lyons/emch361/06s/DIC-McNeill.pdf>
50. Bruck, A., McNeill, S., Sutton M., & W.H. Peters. Digital Image Correlation Using Newton-Raphson Method of Partial Differential Correction. *Experimental Mechanics* **29,** 3, 1989, pp 261-267
51. Dresselhaus, M.G, Dresselhaus G., & P. Eklund. *Science of Fullerenes and Carbon Nanotubes.* Academic Press: New York, 1996.
52. Treacy, M., Ebbesen, T., Gibson J.. Exceptionally High Young's Modulus Observed for Individual Carbon Nanotubes. *Nature* **381**, 1996, pp. 678–80.
53. Yamamoto, N. , Hart, A., Garcia, E., Wicks, S.,Duong, H., Slocum, A. & B.L. Wardle. High-Yield Growth and Morphology Control of Aligned Carbon Nanotubes on Ceramic Fibers for Multifunctional Enhancement of Structural Composites. *Carbon,* **47**, 3, 2009, pp. 551–560
54. Wicks, S. Mechanical Enhancement of Woven Composites with Radially Aligned Carbon Nanotubes (CNTs) . SM Thesis, MIT, 2010.
55. Coleman J., Khan, U., Blau, W., & Y. Gun'ko. Small but Strong: a Review of the Mechanical Properties of Carbon Nanotube–Polymer Composites. *Carbon* **44**, 2006, pp.1624–52.
56. Bauhofer W, Kovacs J.. A Review and Analysis of Electrical Percolation in Carbon Nanotube Polymer Composites. *Composite Science & Technology* **69,** 2009, pp. 1486–98.
57. Moniruzzaman, M., Winey K. Polymer Nanocomposites Containing Carbon Nanotubes. *Macromolecules* **39**, 2006, pp. 5194–205.
58. Hart, A., & A.Slocum Rapid Growth and Flow-Mediated Nucleation of Millimeter-Scale Aligned Carbon Nanotube Structures from a Thin-Film Catalyst *Journal of Physical Chemistry B,* **110,** 16, 2006, pp. 8250–8257.
59. Jones, R. *Mechanics of Composite Materials*. Second Edition. Taylor and Francis: New York. 1999.
60. "HexFlow RTM 6". Hexcel. <http://www.hexcel.com/Resources/DataSheets/RTM-Data-Sheets/RTM6_global.pdf>.2009.
61. Yu, M., Files, B., Arepalli, S, & R. Ruoff. Tensile Loading of Ropes of Single Wall Carbon Nanotubes and their Mechanical Properties. *Physical Review Letters*. **84**, 24, 2000, pp. 5552-5.
62. Cohen, M. Calculation of Bulk Moduli of Diamond and Zinc-Blende Solids. *Physical Review B,* **32**, 1985, pp. 7988–7991.
63. "Principle of Digital Image Correlation." Correlated Solutions. <http://www.correlatedsolutions.com/index.php/principle-of-digital-image-correlation>